

Alpine rock glacier activity over Holocene to modern timescales (western French Alps)

Benjamin Lehmann^{1,2*}, Robert S. Anderson², Xavier Bodin¹, Diego Cusicanqui^{1,3}, Pierre G. Valla⁴, and
5 Julien Carcaillet⁴

¹Université Savoie Mont Blanc, CNRS, EDYTEM, 73000, Chambéry, France

²INSTAAR and Department of Geological Sciences, University of Colorado Boulder, Boulder, CO 80309, USA

³Université Grenoble Alpes, CNRS, IRD, IGE, Grenoble, France

⁴Université Grenoble Alpes, Univ. Savoie Mont Blanc, CNRS, IRD, IFSTTAR, ISTerre, 38000, Grenoble, France

10

Correspondence to: Benjamin Lehmann (lehmann.benj@gmail.com)

Abstract. Active rock glaciers are some of the most frequent cryospheric landforms in mid-latitude high-elevation mountain ranges. Their activity strongly influences the hydrology and geomorphology of alpine environments over short (years to decades) and long (centuries to millennia) timescales. Being conspicuous expressions of mountain permafrost and important
15 water reserves in the form of ground ice, rock glaciers are seen as increasingly important actors in the geomorphological and hydrological evolution of mountain systems, especially in the context of current climate change. Over geological timescales, rock glaciers both reflect paleoclimate conditions and transport rock boulders produced by headwall erosion and therefore participate in shaping high mountain slopes. However, the dynamics of rock glaciers and their evolution over different timescales remain under-constrained.

20 In this study, we adopt a multi-method approach including field observations, remote sensing, and geochronology, to investigate the rock glacier system of the Vallon de la Route (Combeynot massif, western French Alps). Remotely sensed images and correlation techniques are used to document the displacement field of the rock glacier over timescales ranging from year to decades. Additionally, over periods from centuries to millennia, we employ terrestrial cosmogenic nuclide (quartz ¹⁰Be) surface-exposure dating on rock boulder surfaces located along the central flow line of the rock glacier,
25 targeting different longitudinal positions from the headwall to the rock glacier terminus.

The remote sensing analysis demonstrates that between 1960 and 2018, the two lower units of the rock glacier have been motionless, the transitional unit presents an integrated surface velocity of 0.03 ± 0.02 m/a, and the two upper active units above 2600 m a.s.l. show velocity between 0.14 ± 0.08 and 0.15 ± 0.05 m/a. Our results show ¹⁰Be surface-exposure ages ranging from 13.10 ± 0.51 to 1.88 ± 0.14 ka. The spatial distribution of dated rock glacier boulders reveals a first-order
30 inverse correlation between ¹⁰Be surface-exposure age and elevation, and a positive correlation with horizontal distance to the headwall. These observations support the hypothesis of rock boulders falling from the headwall and remaining on the glacier surface as they are transported down valley, and may therefore be used to estimate rock glacier surface velocity over geological timescales. Our results also suggest that the rock glacier is characterized by two major phases of activity. The first

phase, starting around 12 ka, displays a ^{10}Be -age gradient with a rock glacier surface velocity of about 0.45 m/a. Following a
35 quiescent period between ca. 6.2 and 3.4 ka, before the emplacement of the present-day active upper two units. Climatic
conditions have favored an integrated rock glacier motion of around 0.18 m/a between 3.4 ka and present day. These results
allow us to quantify back-wearing rates of the headwall of between 1.0 and 2.5 mm/a, higher than catchment-integrated
denudation rates estimated over millennial timescales. This suggests that the rock glacier system promotes the maintenance
of high rock wall erosion by acting as debris conveyor and allowing freshly exposed bedrock surfaces to be affected by
40 erosion processes.

1 Introduction and motivations

Rock glaciers are important geomorphic structures influencing the evolution of high-elevation mountain environments. They
are lobated or tongue-shaped assemblages of angular rock debris and ice. Rock glaciers move by the deformation of internal
ice, conveying large caliber sediments from high-elevation steep slopes, cirque headwalls to their terminus at lower
45 elevations (Barsch, 1977; Giardino & Vitek, 1988). In the context of current climate change, rock glaciers are considered as
one of the most resilient cryospheric bodies in alpine environments thanks to the insulated effect of their rocky carapace
(Jones et al. 2019). Indeed, they represent an important storage of water supply when mountain glaciers have disappeared
(e.g., Jones et al., 2019). However, in-situ measurements since the last decades have shown rock glacier acceleration and
destabilization associated with increasing air temperature in the European alps (e.g., Marcer et al. 2021). Over geological
50 timescales, rock glaciers participate actively in the development of asymmetrical mountain crests by conveying rock from
leeside headwalls (where rockfall is the primary source of debris) to lower elevations in the valley (Gilbert 1904; Johnson,
1980). Although rock glaciers have received considerable attention in the last couple decades, being catalogued in several
geographic areas (see Jones et al., 2019 for latest review), the formation and evolution of rock glacier are still a subject of
debate, with two main holistic views (see Haeberli et al., 2006; Berthling, 2011). On the one hand, rock glaciers are seen as
55 periglacial features in which ice forms, ice content increases within debris interstices, forming an ice-rock mixture that
creeps by the influence of gravity and sufficient slope (e.g., Wahrhaftig & Cox, 1959; Ikeda et al., 2008). On the other hand,
rock glaciers are thought to result from the remnants of glaciers with a deforming ice core that are being protected by a
continuous debris cover (e.g., Whalley, 1974; Monnier and Kinnard 2015; Anderson et al., 2018).

The development of rock glaciers is a long process taking few decades to thousands of years (e.g., Berthling, 2011). Their
60 morphology, activity and dynamics reflect present and past climates (i.e., temperature and precipitation fluctuations) and
geomorphological forcing (rock and snow avalanching, bedrock structural patterns; Ikeda and Matsuoka, 2006; Kellerer-
Pirklbauer & Rieckh, 2016; Jones et al., 2019). Rock glacier activity is categorized between active, transitional, and relict
modes, and has been recently updated based on geomorphological indicators (Delaloye & Echelard, 2020). An active rock
glacier presents movement in most of its surface whereas a transitional rock glacier will present low movement only
65 detectable by *in-situ*/remote sensing measurement and/or restricted to non-dominant areas. Finally, a relict rock glacier has

no detectable movement and no morphological evidence of recent movement and/or ice content (Delaloye & Echelard, 2020). Rock glaciers have been documented in the European Alps to accelerate with increasing temperature (Delaloye et al., 2010; Kellerer-Pirklbauer, 2017; Wirz et al., 2016; Eriksen et al., 2018; Kenner et al., 2018; Marcer et al., 2021) but when the ice content falls below a critical saturation threshold, rock glaciers stop creeping, turning from active into transitional and eventually relict mode (Sandeman & Ballantyne, 1996). Their activity is also controlled by the geomorphology of the surrounding topography. For instance, it has been suggested that when the rock boulder delivery rate and debris/ice incorporation become insufficient to sustain the insulation of the ice-rich part, the activity of the rock glacier will decrease and stop regardless of the rock glacier thermal state (Amschwand et al., 2021).

The relationships between external forcings and the activity of rock glaciers need to be better understood. Consequently, their past activity and in particular past vs. modern rock glacier surface velocity estimates must be quantified from annual to millennial timescales. This will allow us to assess how ongoing climate change has and will affect rock glaciers. Analytical advancements over the past decades have allowed significant progress based on remote sensing tools for monitoring changes on high-mountain landforms (e.g., Necsoiu et al., 2016; Vivero & Lambiel, 2019; Blöthe et al., 2021; Robson et al. 2022). Indeed, methods such as LiDAR (Micheletti et al., 2017), InSAR (i.e., Liu et al., 2013; Barboux et al., 2014; Strozzi et al., 2020), aerial photogrammetry (i.e., Kaab et al., 1997) and unmanned aerial vehicle systems (i.e., Dall'Asta et al., 2017; Vivero & Lambiel, 2019) have remarkably improved the temporal and spatial resolution of surface velocity surveys for rock glaciers. Recent studies have shown the feasibility of using high-resolution digital elevation models (DEMs) and orthorectified images produced from historical aerial and satellite images to reconstruct the surface velocity of rock glaciers over the last seven decades (Fleischer et al. 2021; Vivero et al. 2021; Kääh et al. 2021; Cusicanqui et al., 2021). Extrapolations from short-term surface velocities have been used to estimate the rock glacier formation time and to reconstruct their activity over longer timescales (Kaab et al., 1997; Frauenfelder and Kääh, 2000; Bodin, 2013). However, it remains difficult to assess such extrapolations and to accurately constrain the long-term dynamics and morphological changes of rock glaciers without reliable estimates over centennial to millennial timescales.

To improve our understanding of rock glacier long-term dynamics and potential forcing mechanisms, relative and absolute dating methods have been applied on both active and relict rock glaciers (e.g., Haeberli, 2013; Amschwand et al., 2021). In rare cases, radiocarbon dating has been used on lacustrine sediments or trees buried by rock glaciers (Paasche et al. 2007) or on vegetal macrofossils found in old permafrost cores from a rock glacier (Krainer et al. 2015). Schmidt-hammer methods have been employed to estimate the surface exposure age of boulders from numerous rock glaciers (European Alps, Pyrenees, Norway, Island and New Zealand) but such an approach requires local calibration surfaces and often only provides relative dating (e.g., Böhlert et al., 2011; Scapozza et al., 2014; Matthews & Wilson, 2015; Winkler & Lambiel, 2018). Similarly, lichenometry has been applied successfully on rock glaciers with stable rock boulders at the surface, although absolute dating requires calibration of this technique (Konrad and Clark, 1998; Galanin et al., 2014). Optically stimulated luminescence has been used to quantify the travel time of buried fine sediments in rock glaciers (Swiss Alps), but large

uncertainties potentially coming from pre-burial bleaching of fine sediments make this approach challenging to apply at
100 larger scale (Fuchs et al. 2013).

Terrestrial cosmogenic nuclide (TCN) dating has been successfully applied to constrain the exposure time of rock boulders
at the surface of relict rock glaciers and their stabilization in the European Alps (Hippolyte et al., 2009; Steinemann et al.,
2020), the Iberian Peninsula (Rodríguez-Rodríguez et al., 2017; Andrés et al., 2018; Palacios et al., 2020; García-Ruiz et al.
2000), Scotland (Sandeman and Ballantyne, 1996) and Iceland (Fernández-Fernández et al., 2020), demonstrating their
105 potential as independent paleoclimate archives to reconstruct past permafrost development and to identify activity phases of
rock glacier (Andrés et al. 2018). Cossart et al. (2010) combined ^{10}Be surface-exposure dating and weathering rind thickness
to document three main generations of rock glacier in the Southern French Alps. Recently, two studies (in Iceland and
Switzerland) have applied TCN dating on rock glacier systems composed of both active and relict units (Fernández-
Fernández et al., 2020; Amschwand et al., 2021), showing deactivation and stabilization of the rock glacier at lower
110 elevations and further distance from the headwall.

The onset of rock glacier development in the high-elevation parts of the European Alps is thought to have started after the
onset of glacier retreat following the Last Glacial Maximum (around 19-18 ka in the European Alps, e.g., Ivy-Ochs, 2015;
Monegato et al., 2017; Lehmann et al., 2020). Chronologies of rock glacier development in the Alps of Austria, Central
Switzerland and France have shown different rock glacier generations: during the Lateglacial period (ca. 16 ka; Steinemann
115 et al. 2020), during or shortly after the Younger Dryas (ca. 12 ka; Cossart et al. 2010; Steinemann et al. 2020; Charton et al.,
2021) and during the Late Holocene (Amschwand et al. 2021), probably at the end of Subboreal period (5.2/5.0 - 4.3/4.2 ka;
Cossart et al., 2010) when the high-elevation cirques became ice-free.

The goal of this study is to reconstruct the activity and the surface velocities at different timescales of the rock glacier system
of the Vallon de la Route (Combeynot massif, western French Alps). A remote-sensing approach utilizing image correlation
120 over photogrammetric products allows us to reconstruct the surface displacement field of the rock glacier over the last six
decades. Over longer periods (10^3 to 10^4 years), we apply TCN dating (quartz ^{10}Be) to rock boulder surfaces at different
positions along the central flow line of the rock glacier, from its terminus to its highest part, allowing the conversion of the
 ^{10}Be surface-exposure ages into long-term surface displacement estimates. By discussing our estimates of rock glacier
surface kinematics at different timescales, we show that it is possible to reconstruct the history of past activity of the rock
125 glacier, and to use rock glaciers as independent paleoclimate and paleo-geomorphological proxies revealing the evolution of
alpine environments.

2 Study site

The Combeynot massif (45°0N - 6°2E) represents the north-eastern part of the Ecrins Pelvoux massif, located in the western
French Alps (Figure 1a). The Ecrins Pelvoux massif presents high alpine topography, with its highest summit being the only
130 one above 4000 m a.s.l. (Barre des Ecrins, 4101 m a.s.l.) and valley bottoms around 1000-1500 m a.s.l. Widespread U-

shaped valley profiles, hanging valleys and glacial trimlines illustrate the imprint of Quaternary glaciations on the massif (Delunel et al., 2010; Valla et al., 2010; Le Roy et al., 2017). Paleo-glacier reconstructions since the Last Glacial Maximum have been previously constrained using mapping, interpolation of glacial features and TCN dating applied on moraine deposits and glacially-polished bedrock surfaces (Delunel, 2010). Evidence for Egesen stadial readvances (the alpine counterpart of the Younger Dryas) have been mapped and dated in several catchments of the massif (e.g., Coûteaux & Edouard, 1987; Charton et al., 2021; Chenet et al., 2016; Hofmann et al. 2019). Based on surface-exposure dating of moraine deposits, glacial advances in the Ecrins Pelvoux massif have been identified from the Lateglacial to the Early Holocene (around 11 ka, Hofmann et al. 2019). Glacial advances during the Neoglacial (from ca. 4.3 ka) have also been reconstructed (Le Roy et al., 2017). Modern glacierized terrain is characterized by small cirque and slope ice bodies covering 68.6 km² in 2009 (Gardent et al., 2014). The two largest valley glaciers remaining today are the Girose Glacier (5.1 km²) and the Glacier Blanc (4.8 km²); most of the other glaciers are cirques or debris covered (Gardent et al., 2014; Figure 1b in Le Roy et al., 2017).

Ranging from 1670 to 3155 m a.s.l., the Combeynot massif hosts 33 active and transitional rock glacier systems and 38 relict rock glaciers (Bodin, 2013). These landforms range from 2000 to 2850 m a.s.l.; the mean elevation of the rooting zones of active rock glaciers is about 2700 m a.s.l., whereas the mean elevation of their frontal positions is 2620 m a.s.l. (Bodin, 2013). The Laurichard rock glacier, on the northern side of the Combeynot massif (Figure 1a), is the site of one of the longest geodetic surveys for surface velocity in the European Alps (since the late 1970s; Francou & Reynaud, 1992; Thibert et al., 2018).

The Combeynot massif comprises a slice of granitic intrusion confined in volcanic-sedimentary gneiss; a flysch layer of the ultra-Dauphinoise zone locally covers its eastern side (Barbier et al., 1973). The characteristic macro-crystalline scale fragility of the crystalline bedrock can be related to Pre-Hercynian hydrothermal activity. A network of NNW/SSE faults and a high density of diaclases cut the Combeynot massif, producing meter and sub-meter scale jointing of the bedrock (Francou & Reynaud, 1992). Thick superficial deposits (mostly coarse material) are the consequence of gravitational and nivo-periglacial processes (cryoclastic and avalanche activity; Francou, 1982).

From a present-day climatic point of view, the Combeynot massif is located in the transition zone between areas influenced by the Mediterranean climate and areas with a more Atlantic climate. Consequently, the local climatic setting is characterized by western frontal incursions and rainfall coming from the Italian side of the Alps and summer periods with low rainfall (Bodin, 2013). Cusicanqui et al. (2021) have performed weather reanalysis of data provided by the S2M (SAFRAN data from Durand, Giraud, et al., 2009; Durand, Laternser, et al., 2009; Vernay et al., 2020). Their results show annual average temperature of $1.3 \pm 0.76^\circ\text{C}$ and snowfall of 791 ± 169 mm/yr for the period 1958-2018 at the Laurichard site (elevation 2400 m a.s.l., northern exposure, 20° slope; Cusicanqui et al., 2021). The average air temperature for the 1958–1990 period is 1.0 against 1.7°C for the period 1991–2018, revealing a change trend of +0.23°C per decade (Cusicanqui et al., 2021). Inversely, the mean number of days of snow cover during winter went from 221 for the 1958-1990 period to 200 for the 1990-2018 period (Cusicanqui et al., 2021).

165 The Vallon de la Route catchment is occupied by neither debris-free nor debris-covered glaciers, but is sheltering a rock glacier system of about 0.674 km². The total catchment area is about 4.41 km², is southwest facing and ranges from 1960 to 3155 m a.s.l. It is bounded upstream by the highest peaks of the massif, the Tete de Pradiou (2879 m a.s.l.), the Roc Noir de Combeynot (3112 m a.s.l.) and the West Pic of Combeynot (3155 m a.s.l.), and downstream by the torrent of the Rif de la Planche (Figures 1a-b). The rock glacier system is overhung by a debris source with area of about 5.351 ×10⁵ m² composed of leucogranitic bedrock (Figure 1b). Geoelectrical measurements (performed in 2006) on the rock glacier have shown that the active layer reaches a maximum thickness of 9 m at 2630 m a.s.l., and that the ice-rich layer does not exceed 15 m and may consist of ice-cemented debris, with occasional layers of higher ice contents (Bodin, 2013). The rock glacier system of the Vallon de la Route (Figure 1) was chosen because it presents the ideal attributes of a rock glacier for this study, namely (i) it has an active snout and sharp edges, (ii) its total length of order of 1 km long, (iii) its situation in the middle of a valley, and (iv) it has one single bedrock type in the headwall source (i.e., leucogranite).

3 Methods

A multi-method approach combining geomorphological mapping and identification, remote sensing, and geochronology was used to reconstruct the history of activity of the rock glacier system of the Vallon de la Route (Combeynot massif, western French Alps).

180 3.1 Geomorphological mapping/identification and image correlation

3.1.1 Geomorphological mapping/identification

Geomorphological recognition was performed using the protocol described in the “Towards standard guidelines for inventorying rock glaciers, Baseline concepts” of the International Permafrost Association Action group for rock glacier inventories and kinematic (RGIK 2020). *In-situ* visual inspection such as observation of the steepness of the front, description of ridge and furrow topography, size and shape distribution of the debris cover, together with using a high-resolution LiDAR Digital Surface Model (DSM, 0.5-m resolution) survey realized by SINTEGRA and landscape image analysis, were performed to geomorphologically classify the different landforms and their connection with each other. Five units (I, II, III, IV and V) were identified from bottom to top according to *in-situ* geomorphological observations such as their elevation, their slope, their vegetation cover, the continuity, and apparent activity of their landforms (elevation, average slope and covered area were determined using the 0.5-m LiDAR high resolution DSM; Figures 1, 2, 3 and 4). Units are separated by either ridge and furrow topography or front, which are the expression of the gravity-driven buckle folding of rock glacier morphology (Frehner et al., 2015). In the present study, we focus our sampling strategy on 13 ridges annotated from A to M (Table 1 and Figures 2 and 6).

3.1.2 Orthomosaic production

195 The reconstruction of the rock glacier surface displacement over decade timescales is done using image correlation protocol between different orthomosaics. Here, we compared timeseries of 2 different orthomosaics (1960 and 2018). The oldest one, acquired on August 22, 1960, was generated using historical aerial photographs (with 3 black and white film images of 0.59 m of resolution) collected from the French National Institute of Geographic Information and Forestry (IGN, www.remonterletemps.ign.fr). The orthomosaic of 2018 was computed using 3 stereo Pléiades 0.7-m resolution acquisition
200 (acquired on August 12, 2018) using Ames Stereo Pipeline (ASP) (Shean et al. 2016). ASP uses rational polynomial coefficients (RPCs) provided with the Pléiades images, eliminating the requirement of a large number of high accuracy GCPs (ground control points). Orthomosaics were computed with Agisoft Metashape (version 1.6) software using ground control points (the same 14 GCP for both orthomosaics) with coordinates collected from the IGN map service (www.geoportail.fr) and elevations using a high-resolution LiDAR DSM (0.5-m resolution) survey realized by SINTEGRA
205 (August 17, 2012). Details on coordinates of the GCPs are given in Figure A1 and Table A1. The orthomosaics were then co-registered using previous LiDAR high-resolution DSM and following Nuth & Kääb (2011) methodology, they were then shifted (translation-only) with co-registration values (x and y displacements). All original orthomosaics were resampled at a 0.5-m resolution and set in a common 3465×3541 -pixel grid system.

3.1.3 Image correlation for surface displacement measurement

210 The 2D displacements of the rock glacier between orthomosaic pairs (1960 and 2018) were computed using the IMCORR module within the SAGA toolbox in QGIS (Scambos et al., 1992). The feature-tracking algorithm retrieves pixel patterns between two georeferenced images and attempts to match small subscenes (called ‘chips’) and produces shapefiles (points and lines) containing the 2D surface displacements. The program uses a fast Fourier transform-based version of a normalized cross-covariance method (Scambos et al., 1992). In the present study, several parameters of the algorithm were tested before
215 settling on the following: search chip size = 128 pixels; reference chip size = 64 pixels; grid space = 10 m.

The obtained surface displacements were first filtered with a threshold of 100 pixels for error on x and y direction estimates (IMCORR xerr and yerr values) removing about 1% of the initial values. We then manually filtered according to (a) different local spatial coverage and artifacts (e.g., related to random local similarity of the coarse blocky surface; Bodin et al., 2018), (b) lack of consistency of the displacement between neighboring vectors (difference $>30^\circ$), and (c) outlier displacement
220 values (Cusicanqui et al., 2021). Finally, 5.4% of the points were removed. The $\pm 1\sigma$ variability is calculated using all the pixels for each unit together with the median displacement. The quality of the results mentioned above is assessed through two analyses. First, the displacements obtained on the rock glacier system are compared to the measured displacements of 6 control areas where no displacement should be observed. Details of those control areas are given in Figures 3, A1, A2 and Table A3. These control areas were chosen to be outside of and around the rock glacier system and out of the scree field. The
225 absence of movement (solifluction, creeping, landsliding) was determined by visually inspecting historical aerial

photographs collected from the IGN-France and the two orthomosaics. In a second time, the potential mismatches between 11 control points between the two orthomosaics have been manually measured. Those manual control points were chosen on topographic features of the surface of our studied area (blocks, cliff structures) and their stability was estimated using the historical aerial photographs collected from the IGN-France.

230 **3.2 ¹⁰Be surface-exposure dating**

TCN surface-exposure dating is based on the observation that when cosmic rays reach the Earth's surface, they produce cosmogenic isotopes in specific targets, such as the production of Beryllium-10 (¹⁰Be) in quartz minerals (e.g., Gosse & Phillips, 2001; Lifton et al., 2014). The in-situ production of ¹⁰Be in quartz occurs predominantly within a few meters of Earth's surface and decreases exponentially with depth such that by knowing a measured concentration of ¹⁰Be in the first centimetre of a rock surface and the local production rate of ¹⁰Be in such a rock, it is possible to calculate an apparent surface exposure age (Portenga and Bierman, 2011). In this section, we detail how samples were collected, prepared, and analyzed, and we explain how external processes affecting the dataset can be estimated.

3.2.1 Sampling

The samples were collected with approximately 0.5 kg of rock material from the 13 ridges of interest (Tables 1 and 2; Figure 6). For 6 of these ridges (A, D, G, I, K and L, Table 1 and Figure 6) two different boulders were sampled to evaluate the reproducibility of our dating approach (Figure 2c). The boulders were chosen following the central flow line which was defined to be both at the center of the rock glacier width and perpendicular to the main ridge and furrow topographic ridges (red lines in Figures 3 and 6), from the terminus to the high-elevation active lobes of the rock glacier system. Sampled boulders were chosen on the top of the ridges to minimize topographic shielding, snow-cover effect, and complex exposure histories (i.e., sediment or clast cover, late exhumation; Figures 2c-d). Suitable boulders are large (>1.5 m) and in a stable position (Figures 2c-d). Appropriate rock surfaces do not show signs of intense weathering or recent chipping. Sampling was done using a hammer, a chisel, and a small electric circular saw over 4 days (28/09/20-01/10/20). The sampling details of each rock boulder including coordinates, elevation, distance to the headwall, height of the sample from the ground, size of the boulder and topographical shielding are summarized in Tables 1 and 2.

250 **3.2.2 TCN preparation and ¹⁰Be measurement**

Samples were crushed and sieved to retain the 200-500- μ m grainsize fraction. Beryllium extraction was performed at the GTC platform (ISTerre, France) using a chemical protocol adapted from Brown et al. (1991) and Merchel & Herpers (1999). Magnetic separation was used to isolate the quartz fraction, followed by successive leaching in an H₂SiF₆/HCl mixture. In order to speed up the purification of quartz and save leaching cycles, magnetic separation with fine magnetite powder was performed between leaching cycles, to remove partially altered minerals. Meteoric Be purification was achieved with three sequential dissolutions using diluted HF (Kohl & Nishiizumi, 1992). The purified quartz samples (13-26 g for each

individual sample) were completely dissolved in concentrated HF after being spiked with ~510 mg of a 998 mg/L Be carrier solution (Scharlab ICP Standard, batch 16107901) to fix the $^{10}\text{Be}/^9\text{Be}$ ratio (Table 2). After HF evaporation, perchloric and nitric acids were added and evaporated to remove organic compounds and fluorides. Beryllium was extracted by successive alkaline precipitations of $\text{Be}(\text{OH})_2$ alternated with separation on anion and cation columns. Samples were then oxidized at 700°C for 1h and the final BeO mixed with Nb powder and loaded into nickel cathodes. ^{10}Be concentration were measured at ASTER national facility (Cerege, France) against standard BeO_STD-11 ($1.191 \pm 0.013 \times 10^{11}$; Braucher et al., 2013) and were corrected for the full process blank with a $^{10}\text{Be}/^9\text{Be}$ ratio of $6.278 \pm 0.534 \times 10^{-15}$.

3.2.3 Surface-exposure age calculation

Surface-exposure ages were computed with the CREp online calculator (Martin et al., 2017) using the LSD scaling scheme (Lifton et al., 2014), the ERA40 atmospheric model (Uppala et al., 2005) and the Lifton VDM 2016 geomagnetic database (Pavón-Carrasco et al., 2014). We used the Chironico landslide production rate (with sea-level high-latitude value of 4.16 ± 0.10 atoms g/a; Claude et al., 2014), scaled according to the sample longitude, latitude and elevation.

The production rate was corrected for sample thickness (Table 2) and density (2.75 g/cm^3). Shielding correction includes the topographic shielding due to surrounding landscape and the dip of the sampled surface calculated with the online calculators CRONUS-Earth (Balco et al., 2008, <http://hess.ess.washington.edu/math>). In addition, we explore the influence of snow-cover attenuation using the (Gosse & Phillips, 2001) equation with snow density of 0.3 g/cm^3 and an attenuation length for fast neutrons in snow of 150 g/cm^2 (Delunel et al., 2014). According to a previous study dating a rock avalanche less than 1 km north of our site (Chenet et al. 2016), we use an estimate of 50 cm cover of snow for 6 months of the year, values that are most often cited in the literature for the Alpine regions for these altitudes (Hormes et al., 2008; Susan Ivy-Ochs et al., 2006; Kelly et al., 2004; Schindelwig et al., 2012; Wirsig et al., 2016; Chenet et al., 2016).

3.2.4 Inheritance/pre-exposure estimation

The measured ^{10}Be concentrations of rock glacier boulder surfaces should always be interpreted with caution as multiple external processes can affect them. Surface erosion can cause a depletion of ^{10}Be concentration at the rock boulder surface, as can complex exposure histories (discontinuous exposure, snow/sediment cover), both of which would lead to an underestimation of the “accurate” ^{10}Be surface-exposure age. Note that, in this study we do not consider the effect of boulder surface erosion; consequently, our reported ^{10}Be surface-exposure ages must be seen as minimum estimates. On the other hand, inheritance (i.e., headwall pre-exposure before rock collapse on the rock glacier), will lead to overestimation of the ^{10}Be surface-exposure age. We choose two approaches to quantify the potential inheritance/pre-exposure bias. The first one is to use linear regression between ^{10}Be surface exposure age and distance to the headwall. Without inheritance, boulders located at the contact between the headwall and the talus slope (distance to the headwall equals to zero) should have a negligible ^{10}Be concentration. Any ^{10}Be concentration given by linear regression at the headwall would be interpreted as time spent (inheritance) in the cliff before the rock fall event. The second approach is to compare the ^{10}Be concentration of

290 samples collected on the same ridge. Any difference in ^{10}Be concentration could be interpreted as a difference in time spent
on the cliff face before the rock fall event. In this case, the inheritance time is calculated using the ^{10}Be concentration
difference between replicates using the ^{10}Be production rate at the elevation of 2997 m a.s.l. (corresponding to the middle
elevation of the cliff source).

295

3.3 Surface velocity estimation

Armed with both geochronological and remote sensing datasets, the time-averaged surface velocity of the rock glacier
system can be estimated. When considering ^{10}Be surface-exposure dating, the mean surface speeds are calculated by dividing
300 the distance to the headwall of either the individual sample or the unit (mean distance to the headwall evaluated at all pixels
inside within the unit limits) by their corresponding individual or median ^{10}Be surface-exposure ages. Here we assumed that
the ^{10}Be surface-exposure age represents exposure between the time of the rockfall event that delivered the block to the
surface of the headwall/talus transition and its arrival at the sample site. In contrast, the modern velocities derived from
remote sensing analysis are calculated by dividing the measured displacement or the median values for each unit, by the time
305 between the two orthomosaics, in this case 58 years (1960-2018 period).

4 Results

According to the geomorphological mapping and identification approach described in section 3.1.1, the rock glacier system
was divided into five different units, in which we apply the approach presented above to reconstruct the chronology of the
rock glacier displacement since the onset of the Holocene.

310 4.1 Field observations

At the lower part of the rock glacier system, the units I and II, with elevation ranges of 2585-2521 and 2718-2557 m a.s.l.,
respectively (and covering about 0.214 and 0.177 km², respectively), clearly display relict morphologies with no
geomorphological evidence of recent surface movement. Their metric to pluri-metric debris layers are highly covered by
superficial material and vegetation (Figures 2c). The unit III, spanning from 2685 to 2556 m a.s.l. and covering 0.155 km²,
315 was evaluated to be transitional. Indeed, the evidence of downslope movement is less visible (but still detectable) than for
units IV and V, as the ridge-and-furrow topography is less prominent. The unit IV (ranging from 2735 and 2626 m a.s.l.) and
the unit V (ranging from 2867 and 2685 m a.s.l.) were classified as active and cover areas of about 0.542 and 0.729 km²,
respectively. They display evidence of downslope creep movement such as steep fronts, strongly marked ridge-and-furrow
topography, absence of vegetation cover and active layers composed of decimetric to metric angular debris. These two units
320 are talus-connected, meaning that they are part of a downslope sequence including headwall – talus slope – rock glacier

(Figures 2a-b). The delivery of debris is likely accomplished by rockfall activity, surface runoff, debris flow and/or avalanche events from the headwall bedrock. The horizontal limit between the talus slope and rock glacier units can be estimated with about 50 m of uncertainty. This top to bottom organization from active, to transitional and relict units is common in alpine settings. The surfaces of the boulders evolve along the rock glacier longitudinal transect. The boulders of units I and II are rounded and display quartz phenocrystals, a rugged surface, millimetric weathered crust and about 80% lichen cover (Figure 2c). On the other hand, boulders of the units IV and V are more angular, with only about 10 to 30% of lichen cover and less obvious surface weathering features (Figure 2d).

4.2 Image correlation

As described in section 3.2, we used a pair of orthomosaics to reconstruct surface displacement of the rock glacier system. The 1960-2018 pair is the most adapted to reconstruct the activity of the rock glacier system over decadal timescales. As the aim of this study is to compare modern to Holocene rock glacier activity, we focus on the integrated displacement over the longest and best-quality time series available, instead of focusing on shorter-scale variations in surface displacement over modern timescales (e.g., Cusicanqui et al., 2021). Figures 3, 4 and 5 present the results obtained using the IMCORR feature-tracking module. The surface displacement of the control areas (dashed outlined area in Figures 3 and A1) within stable terrain shows a median displacement of 0.79 ± 0.43 m (Figures 4g, A2 and Table A3). This value represents the accumulation of error from the orthomosaic production and the image correlation procedure. The quality of the orthomosaic production can be assessed using the statistics on the GCPs showing a median absolute error of 0.57 ± 0.34 m (Table A1) and the manual control points presenting a median mismatch distance between the two orthomosaics of about 1.04 ± 0.45 m (Figure 4h and Table A2). This last value, being the highest of the three error estimations, is used hereafter as a threshold value to control the confidence level of our remote sensing analysis, and should be considered as the detection limit. Consequently, all rock glacier areas showing surface displacement lower than 1.04 m are consequently considered as below the detection level (dashed area in Figure 5).

Surface displacements calculated over the entire rock glacier system for the last 58 years (i.e., between 1960 and 2018) show a maximum value of 20.4 m, with a median displacement of 1.3 m and a standard deviation of 2.0 m over the entire rock glacier area (Figures 3, 4f and Table A3). Note that those estimates integrate displacements over 58 years, and do not allow us to assess whether the displacements have been steady or not. The spatial distribution (Figure 3) and the longitudinal transect (Figure 5a, location by red line in Figure 3) show that significant surface displacements are concentrated in the upper part of the rock glacier system. Indeed, units IV and V show median surface displacements over the 1960-2018 period of 8.5 ± 2.9 m and 8.3 ± 4.9 m, respectively (values calculated for all the values inside each unit outline; Figures 3, 4d-e and Tables 4, A3). This agrees with our classification as “active” from geomorphological observations (Figure 2 and Section 4.1). The unit III presents surface displacements of 1.9 ± 1.4 m (Figures 3, 4c and Tables 5, A3), which is above the detection limit. Our classification of transitional activity (Section 4.1) thus seems appropriate. Finally, units I and II, with median displacement of 1.2 ± 0.4 and 0.9 ± 0.6 m, respectively, are similar within $\pm 1\sigma$ and below the detection limit (Figures 3, 4a-b

and Tables 4, A3). These parts of the rock glacier system can thus be considered to be immobile over this period and correspond well with the relict classification determined from geomorphological observations (Section 4.1). The rock glacier becomes inactive around 945 m from the headwall, corresponding to an elevation of about 2600 m a.s.l. Also, two displacement peaks can be observed in the upper part of the rock glacier system (Figures 3 and 5a), one in unit IV and another in unit V, potentially indicating different debris sources for the two units.

4.3 Surface-exposure dating results

Figures 6 and 7, together with Tables 2-4, present the analytical results of ^{10}Be surface-exposure dating for each individual boulder sample, as well as for statistics within ridges and units. Our ^{10}Be -age results range from 13.10 ± 0.51 to 1.88 ± 0.14 ka for the entire dataset. The correction for snow-cover shielding ranges between 7 and 9% between samples. In view of the controversy over whether wind could remove snow from moraine/rock glacier ridges during the Holocene period (Federici et al., 2008; Schimmelpfennig et al., 2014; Moran et al., 2016; Chenet et al., 2016), we refrain from correcting the output ^{10}Be ages for snow cover in the following discussion. This implies that our reported ^{10}Be ages, with neither snow-cover nor surface-erosion correction, should be considered as minimum estimates.

Our results clearly reveal a first-order inverse correlation between ^{10}Be surface-exposure age and elevation, and a positive correlation between ^{10}Be surface-exposure age and horizontal distance from the headwall (Figure 7). These correlations remain valid when we consider the median values of the ^{10}Be surface-exposure ages for each unit (Figures 7c-d, Table 3) and ridge (Figure A3, Table 4).

Visual inspection of the ^{10}Be -age dataset allows the identification of two clusters: cluster 1 includes the lowermost units (I, II and III) whereas cluster 2 combines the highest units IV and V. Cluster 1 presents ^{10}Be ages between 9.25 ± 0.40 and 13.1 ± 0.51 ka and cluster 2 shows ^{10}Be ages between 1.88 ± 0.14 and 4.88 ± 0.29 ka. These results agree with the geomorphological classification we proposed for these rock glacier units, in which units I and II are viewed as relict, unit III as transitional, and units IV and V as active.

To assess the reproducibility of our dating approach, we sampled 2 different boulders on 6 of the rock glacier ridges (A, D, G, I, K and L; Figures 2d, 6 and 8). The minimum and maximum horizontal distances between two replicates are about 8 and 82 m for ridges D (samples VR12 and VR13) and L (samples VR18 and VR19), respectively; a minimum elevation difference of about 2 m for ridges G (VR8 and VR9) and A (VR16 and VR17) and a maximum elevation difference of 14 m for ridge D (Figure 6 and Tables 1 and 2). Significant variability in ^{10}Be surface-exposure age occurs at the ridge scale, although it does not affect the correlations discussed above (Table 3 and Figure 7). Ridge K presents the higher age variability (99%, ^{10}Be surface-exposure ages of 1.32 ± 0.21 and 4.88 ± 0.29 ka for samples VR2 and VR3, respectively, Table 3 and Figure 8d). The age variability for the other ridges is correlated with elevation and anticorrelated with distance to the headwall (26%, 13%, 10%, 8% and 2% of age variability for 2 samples per ridge for ridges L, I, G, D and A, respectively, Table 3 and Figure 8). Only ridge A displays variability that is smaller than the absolute uncertainty on individual ^{10}Be surface-exposure ages and may therefore be considered non-significant. The same pattern is observable for variability at the

scale of the units (Table 4 and Figure A4). Finally, samples from cluster 2 show much higher variability than samples from cluster 1.

390 **4.4 Surface velocity**

Figure 9 and Table 4 compile and illustrate the rock glacier surface velocities calculated from the ^{10}Be surface-exposure dating and from the correlation of aerial and satellite orthomosaics. The surface velocities based upon ^{10}Be surface-exposure dating range from 0.08 ± 0.004 to 0.33 ± 0.05 m/a with a median value of 0.13 m/a (Figure 9). When we calculate the median value for the different units, the surface velocities range from 0.09 ± 0.01 to 0.18 ± 0.11 m/a (Table 4).

395 For the remote-sensing analysis, we define a detection limit of 0.02 m/a corresponding to the median mismatch distance between the manual control point integrated over the 1960-2018 period (Figures 4h, 5 and Table A2). As the displacements of units I and II show surface velocities identical to the detection limit, we consider them immobile over the six last decades. Measurable motion occurs above 2600 m a.s.l., with velocities of 0.03 ± 0.03 m/a in unit III. The upper units display higher velocities of the same order, about 0.15 ± 0.05 and 0.14 ± 0.08 m/a for units IV and V, respectively (Figure 9).

400 **5 Discussion**

The surface-displacement reconstructions of the rock-glacier system of the Vallon de la Route from both image correlation and ^{10}Be surface-exposure dating provide interesting and original insights on the applicability of such methodology on rock glacier landforms. It also suggests potential feedback between rock glacier activity, past climate, and geomorphological processes such as headwall erosion. Here we discuss the implications of the results obtained at the Vallon de la Route rock glacier system.

405 **5.1 Inheritance/pre-exposure and loss/incomplete exposure**

The evaluation of the source of debris elevation and the estimation of the inheritance/pre-exposure of investigated boulders was performed using linear regression of the ^{10}Be dataset presented in Figure 7, as explained in Section 3.4 (Amschwand et al., 2021). For instance, when we calculate the intercept of cluster 2 regression (i.e., elevation at which the ^{10}Be surface-exposure age is null), we obtain an elevation of 2737 m a.s.l.; whereas if we include all the samples together (red and black dotted lines in Figure 7a, respectively), we obtain 2748 m a.s.l. From our geomorphological observations, the elevation at which the talus slope connects to the headwall is close to 2880 m a.s.l. (mean elevation of the foot of upper headwall), which may safely be considered the elevation at which debris is delivered to the rock glacier. The difference between these elevations could lead to the interpretation that the ^{10}Be surface-exposure ages are underestimated. We argue that this discrepancy can instead be explained by the fact that our sampling strategy targeted the biggest boulder at the surface of the rock glacier, so that the likelihood of any burial event was minimized. The sampled metric and pluri-metric boulders might have rolled farther from the cliff and might therefore be incorporated onto the rock glacier surface at a higher distance/lower

elevation than the present-day limit between the talus and the headwall. The relationship between ^{10}Be surface-exposure age and elevation is also dependent on the relation between elevation and distance along the rock glacier (i.e., hypsometric distribution of the rock glacier surface) and the potential inheritance/pre-exposure effects on the measured ^{10}Be concentrations.

Linear regression between horizontal distance from the headwall and ^{10}Be surface-exposure age (Figure 7b) allows us to quantify potential inheritance/pre-exposure bias (e.g., Amschwand et al. 2021). By considering cluster 2, the samples have experienced inheritance/pre-exposure of about 2.16 ka (intercept of red dashed line in Figure 7b). This assumes that (i) blocks fall at the talus/headwall contact and, (ii) the displacement rate is continuous over the temporal range of the considered ^{10}Be surface-exposure ages. Once again, this inheritance/pre-exposure estimate must be put in proper geomorphic perspective, as units IV and V do not share the same headwall source (with potentially different slope aspects and thus different erosion rates). When regressed individually for units IV and V, the estimated inheritances are about 2.79 and 1.59 ka for units IV and V, respectively. For above calculations, we only used samples from cluster 2, being the youngest and closest to the headwall. Samples from cluster 1, with the oldest ^{10}Be surface-exposure ages and the greatest distances from the headwall, could also involve other biases that include non-continuous displacement rate over this timescale and loss/incomplete exposure due to surface erosion or tilting and burial of the sampled surface.

The variabilities of our ^{10}Be surface-exposure ages of the ridges and the units are lower at low elevation and far from the headwall (Tables 3-4 and Figures 8-A4). A first interpretation is that of the samples whose variability is smoothed between samples during transport and exposure on the rock glacier (cluster 1). We interpret this as highlighting that the events of tilting, burial and/or erosion of the sampled boulders do not strongly influence the reported ^{10}Be surface-exposure ages, and that the variability likely arises instead from differing exposure times on the headwall prior to rockfall delivery onto the rock glacier surface. Secondly, the importance of inheritance/pre-exposure events would have less importance for the oldest ^{10}Be surface-exposure ages than for the youngest ^{10}Be surface-exposure ages. The high variability in cluster 2 of ^{10}Be surface-exposure ages could be explained by variation in ^{10}Be inheritance due to pre-exposure in the headwall. Using the difference in ^{10}Be concentration between replicates, we estimated an inheritance. The calculated age differences are about 0.17 ± 0.01 , 0.67 ± 0.03 , 1.06 ± 0.04 , 0.39 ± 0.03 , 2.88 ± 0.47 , 0.88 ± 0.04 ka for ridges A, D, G, I, K and L, respectively (Table 3). The median value of those results is 0.78 ± 0.97 ka and can now be compared with the inheritance estimate of 2.16 ka derived from using linear regression between ^{10}Be surface-exposure age and distance to the headwall of cluster 2.

We interpret the majority of the observed variability in ^{10}Be surface-exposure ages as representing the stochastic nature of rockfall events. This leads to both different residence times of boulders in the headwall before rock fall, and different sites of incorporation of boulders in the talus/rock glacier system. Interestingly, all sample ^{10}Be surface-exposure ages suggest low inheritance compared to other settings in the European Alps. In the Mont Blanc massif, for example, the more competent granitic spurs result in potential inheritance of >10 ka (Gallach et al., 2018, 2020), with commensurately lower rate of debris supply and lower frequency of rockfall events (see Section 5.3 for discussion about headwall erosion rates).

5.2 Surface velocity comparison and reconstruction

The 1960-2018 rock glacier surface velocities calculated from the correlation of aerial and satellite orthomosaics validate our proposed geomorphological classification for the activity of the different units (units I and II relict, unit III: transitional and units IV and V: active). This activity is occurring above 2600 m a.s.l. While no correlation between the distance from the headwall and the surface velocity is clearly visible; the variability in surface velocity is significantly higher for units IV and V. The difference between units IV and V likely reflects their different debris- and snow-avalanche sources; they may therefore have independent age and surface-velocity profiles. This could therefore lead to an overestimation of the distance to the headwall for unit IV (as the central line is defined with respect to unit V, Figure 6), and by consequence to an overestimation of its surface velocity.

The velocity of the two upper units above 2600 m a.s.l., which show surface velocity of about ~ 0.15 m/a between 1960 and 2018, are slower than the reconstructed surface velocity of the Laurichard rock glacier, located in the adjacent cirque 1 km north to our study site and facing north (Cusicanqui et al., 2021). In this study, the authors quantified an acceleration of the average surface velocity changing from 0.5 ± 0.09 m/a for the 1952–1994 period to 1 ± 0.09 m/a for the period 2013–2017 for this landform ranging from 2430 to 2630 m a.s.l. The difference of activity between the two sites could be explained by the control of insolation and mean annual temperature on the permafrost conditions, which are more favourable to the north facing slopes (Laurichard) than the southeast facing slopes (Vallon de la Route). This has been highlighted by the Permafrost Favorable Index distribution of the area (Marcer et al. 2017). Also, Marcer et al. (2021) have estimated the rock glacier kinematics over the past seven decades for the entire French Alps using aerial orthoimagery. Mean displacement rates increased from 0.3 m/a (for the period from 1948–1952 to 2001–2004) to 0.97 m/a (for the period between 2001–2004 to 2008–2009) to 1.25 m/a (from 2008–2009 to 2015–2017). Note that the values obtained in our study site are below the detection limit of this regional reconstruction (0.52 m/a for the period from 2008-2009 to 2015-2017; Marcer et al., 2021).

The velocity obtained by integrating ^{10}Be surface exposure age over the distance to the headwall, ranging from 0.08 ± 0.004 to 0.33 ± 0.05 m/a, are about the same order of magnitude as that obtained by Amschwand et al. (2021) using the same approach (~ 0.3 m/a). Comparing the surface velocity obtained with our two datasets (orthomosaics correlation and ^{10}Be surface-exposure dating), we see that active units (IV and V) share similar surface velocities between long-term and short-term approaches (blue and red dataset on Figure 9). Integration of the short-term surface velocities over the late Holocene appears to predict well the ^{10}Be surface-exposure ages of investigated rock glacier boulders. This suggests that the climatic and geomorphological conditions controlling the activity of the rock glacier have been stable above 2600 m a.s.l. over the last ca. 5 ka.

These observations should be put in a spatial perspective. The remote sensing analysis results in an estimate of the mean surface velocity over the entire area of the unit. On contrast, the velocity estimated from the ^{10}Be surface-exposure dating was calculated from samples collected at the center of the rock glacier system, where the surface velocity is likely to be the fastest regarding a transversal cross section. The median velocity of the unit will be lower than the maximum centerline

speed, as lower thicknesses at the margins should slow the surface speeds. It is therefore expected that the ^{10}Be -based
485 method would likely yield faster speeds than the remote-sensing method. Consequently, the agreement and relationship
between the two datasets and the two timescales should be interpreted with caution.

5.3 History of rock glacier activity

The Vallon de la Route cirque is occupied by a rock glacier system with well-defined rock glacier geomorphological
attributes such as steep fronts, margins, ridges and furrows topography (Figure 1b and 2). No evidence of former occupation
490 of the cirque by a clean ice or debris covered glacier is visible (no moraine nor polished bedrock surface). Consequently, we
interpret the correlations presented in Section 4.3 between the ^{10}Be surface-exposure age and distance to the headwall to
support the hypothesis that rock boulders originate from the headwall and are then transported downward on the surface of
the rock glacier: the further from the headwall (and the lower the elevation) the boulder is, the older its ^{10}Be surface-
exposure age.

495 Following this reasoning and acknowledging the ^{10}Be surface-exposure age distribution along the rock glacier, we propose a
possible history for the rock glacier activity that includes two pulses of constant surface velocity. Figure 10 presents
schematically our interpretation of the two clusters of ^{10}Be surface-exposure ages according to their distances from the
headwall (Figures 7b and 11b). During a first phase of activity, boulders fall from the headwall onto the surface of the rock
glacier (Figure 10a). The random distance from the headwall at which the boulder is incorporated in the rock glacier is
500 representing the stochasticity of rockfall travel. The ^{10}Be inheritance, corresponding to the residence time of the rock in the
headwall, is also stochastic. As rockfall-derived boulders are transported down-valley, both their ^{10}Be surface-exposure ages
and distances from headwall increase from these initial values (red lines in Figure 10a). When the motion halts (presumably
because the rock glacier thins beyond some threshold thickness), this first phase of activity ends, and boulders remain
stationary while their ^{10}Be surface-exposure ages continue to increase (Figure 10b). During this phase of inactivity, we
505 consider that neither snow nor rock avalanches are active. Finally, a new phase of activity begins at the base of the talus (red
points in Figure 10c), and the new rock glacier overrides the up-valley boulders on the relict rock glacier (shadow points in
Figure 10c). In this conceptual model, we assume that the first phase of activity transported the boulders further downstream
than the second phase of activity.

We therefore argue that cluster 1, corresponding to ^{10}Be surface-exposure ages of units I, II and III, represents a first phase
510 of activity of the rock glacier, and that cluster 2, with units IV and V, represents a second phase of activity. To constrain both
the timing and the surface velocities of these phases of activity, we numerically simulate the evolution of ^{10}Be surface-
exposure ages of boulders during their movement at the surface of the rock glacier (Figure 11b). To represent its
stochasticity, we prescribed the inheritance (b in Figure 10) with random values between 0 and 2.16 ka (as determined in
Section 5.1). In the same way, the distance of incorporation of boulders on the rock glacier surface (a in Figure 10) is
515 randomly sampled between 0 and a maximum of 100 m. In this model, three different times must be prescribed. The
initiation of the first phase of activity is set at 12.1 ka (t_1 in Figure 11a), which is the ^{10}Be surface-exposure median age of

unit I. The second phase of activity is set to start at 3.4 ka (t_3 in Figure 11a) as this is the ^{10}Be surface-exposure median age of unit III and is still active now. Only the time at which the first phase of activity ends cannot be directly extracted from the data (t_2 in Figure 11a). Consequently, we simulate the ^{10}Be surface-exposure age structure of the rock glacier complex for
520 100 values of t_2 ranging from t_3 (3.4 ka) to the youngest age of cluster 1 (i.e., 9.25 ka for sample VR8). The velocity of phase 1 is calculated using the maximum distance a block travelled at the surface of the rock glacier (1720 m) and the activity duration of phase 1 (t_1-t_2). The velocity of phase 2 is fixed at 0.22 m/a, a value calculated using the maximum distance a block travelled at the surface of the rock glacier during this phase (740 m) and the duration of activity (t_3 in Figure 11a).

525 The 100 simulations are evaluated against the measured ^{10}Be concentrations using chi-square per degree of freedom, $\chi_v^2 = \frac{\chi^2}{v}$. The chi-squared is a weighted sum of squared deviations: $\chi^2 = \sum_i \frac{(O_i - C_i)^2}{\sigma_i^2}$ where σ is the variance on our ^{10}Be dataset, O are the observations, and C are the modeled data. The degree of freedom, $v = n - m$, equals the number of observations n minus the number of fitted parameters m (here 4: maximum inheritance, maximum distance of incorporation of a boulder on the rock glacier, initiation of phase 1: t_1 and phase 2: t_3). The likelihood probability function is then calculated as $\mathcal{L} =$
530 $1/\exp(\chi_v^2/2)$ and normalized with its maximum to extract the median value and the standard variation ($\pm 1\sigma$) of t_2 (Figure 11c). The inversion results suggest that the first phase of activity lasted from 12.1 to 6.26 ± 1.96 ($\pm 1\sigma$) ka, with a surface velocity of 0.29 ± 0.15 ($\pm 1\sigma$) m/a. The second phase of activity starts at 3.4 ka and has a surface velocity of 0.22 m/a (Figure 11a). The most recent phase of activity overrides the ^{10}Be surface-exposure ages of the two upper units. We now discuss how these two phases of rock glacier activity can be connected to what is known about the paleo-environmental conditions in the
535 western European Alps.

5.4 Reconstruction of paleo-environmental conditions

In the European Alps, the final Lateglacial period (i.e., Egesen) led to readvance of the mountain glaciers reaching a maximum extent around 12 ka for both the eastern and western Alps (e.g., Susan Ivy-Ochs et al., 2008; Protin et al., 2019; Hofmann et al. 2019). Directly downstream of the Vallon de la Route catchment, ^{10}Be surface-exposure ages of moraines
540 show ages of 13.0 ± 1.1 ka and 12.4 ± 1.5 ka, providing evidence for two stages of glacial advance or standstill at the end of the Lateglacial period (Chenet et al. 2016). In a southern valley of the Ecrins Pelvoux massif, morainic deposits at Pré de la Chaumette (downvalley from Rougnoux Valley) have been dated at 12.5 ± 0.6 ka (Hofmann et al. 2019). Immediately after the onset of the Alpine glacier retreat (12.2 ± 1.5 ka in the same valley, Chenet et al., 2016), several advance episodes lasting ~ 1 ka were identified in the Ecrins massif. Dating in the southern part of this massif has shown glacial activity during the
545 Lateglacial that may have lasted until the Early Holocene before final glacial retreat (around 11 ka, Hofmann et al. 2019). Cossart et al. (2010) reported histories of glacier retreat and rock glacier generation in the Clarée valley (about 10 km to the east of our study site). They identified three generations of rock glacier development during the second half of the Holocene,

ranging in elevation from ~2400 to 2800 m a.s.l. Recent dating of Charton et al. (2021) on two rock glaciers located ~3 km to the north of our site and at an elevation of about 2050 m a.s.l. reveals ^{10}Be surface-exposure ages of ca. 11 ka. They interpreted the ^{10}Be surface-exposure ages as marking the end of activity of the rock glacier.

In the present study, we interpret the ^{10}Be surface-exposure ages as being the sum of its residence time on the headwall cliff, the time spent traveling on the surface of the rock glacier, and the time since deactivation of the relict portion of the rock glacier for the relict units. We argue that rock boulders remain at the surface of the rock glacier while being transported down valley. This is supported by the small variability in ^{10}Be surface-exposure ages obtained from the ridge replicates far from the headwall, which implies little occurrence of tilting and burial events (c.f. Section 5.1). This is also supported by the rock boulder weathering evolution along the rock glacier, which displays more weathered surfaces far from the headwall (c.f. Section 4.1). Consequently, in the Vallon de la Route catchment, the first phase of rock glacier activity appears to start around 12.1 ka from our oldest ^{10}Be surface-exposure age (median value of the unit I). We suggest that this coincides with the final glacier retreat at the end of the Lateglacial period at the onset of the warm period marking the Younger Dryas – Holocene transition (e.g., Liu et al., 2014). The upper mountain catchments and cirques then became free of glaciers, allowing the headwall and scree field to feed a rock glacier with debris thickness sufficient to insulate the ice. In this case, the rock glacier development would be geomorphically-controlled by contrast to a climatic control (Cossart et al., 2010). As presented above, this first phase of activity would have ended around 6.26 ± 1.96 ($\pm 1\sigma$) ka. According to our reconstruction, the second generation of rock glacier development occurred starting at about 3.4 ka. This is earlier than the estimate proposed by Bodin (2013) from the relationship between slope and velocity, based upon an estimated time of 1.7 ka for debris to reach the front of the unit V lying at around 2740 m a.s.l.

Whereas lateral glacier moraines dated using ^{10}Be surface-exposure approach suggest minor but several glacier re-advances between ca. 4.25 and 0.92 ka in the main glacierized valleys of the Ecrins-Pelvoux massif (Le Roy et al. 2017), there is no evidence for glacial re-occupation during the Neoglacial/Little Ice Age periods in the Vallon de la Route. This specific cirque does not share upstream connection with any of the main glacierized valleys of the massif. The headwall and scree taluses were ice free and could therefore feed the rock glacier system with debris and snow avalanches, maintaining the rock glacier during the last 3.4 ka, when the Neoglacial/Little Ice Age climate was favourable for glacier/rock glacier activity.

Consequently, the inspection of the age structure of our rock glacier suggests two episodes of motion (Figure 11a). The first phase, starting around 12.1 ka, displays a gradient in age with rock glacier surface velocity of about 0.45 m/a. The rock glacier activity then declines and stops at 6.26 ± 1.96 ka. By around 3.4 ka, the climate again becomes conducive to rock glacier motion at elevations above 2600 m a.s.l. and the presently active upper two units have been emplaced. Even if climate during the Late Holocene has fluctuated (e.g., Liu et al., 2014), the integrated velocities calculated with the ^{10}Be surface-exposure ages reveal that the surface velocity of 0.18 m/a (Figure 11a) agrees with modern estimates.

580

5.5 Headwall erosion and implications

The reconstruction of the rock glacier activity provides a way to quantify the erosion rate of the surrounding headwalls over Holocene timescales (e.g. Humlum 2000; Amschwand et al. 2021). Bodin (2013) has performed geophysical measurement of the rock glacier area and could determine a maximum thickness of the active layer of about 9 m and a maximum thickness of the ice-rich layer of about 15 m at 2630 m a.s.l. The entire area of the rock glacier is $6.745 \times 10^5 \text{ m}^2$. An approximation of the total volume of debris, considering a total thickness of between 9.5 m (active layer thickness of 5 m and ice-rich layer of 4.5 m thick at 2720 m a.s.l.; Bodin, 2013) and 24 m (combining maximum of active layer thickness of 9 m and ice-rich layer of 15 m thick at 2630 m a.s.l.; Bodin, 2013), gives respectively 3.37×10^6 and $13.49 \times 10^6 \text{ m}^3$. Regarding the low surface velocity estimated between 1960 and 2018, between 0.14 and 0.03 m/a over 42% of the total area (units III, IV and V) and no movement of the other 58% of the total rock glacier area (units I and II), we can assume a negligible ice concentration over the full volume of the rock glacier system. Taking this volume of debris over 12.1 ka (the median ^{10}Be surface-exposure age of unit I), and considering that all boulders are derived from bedrock exposed above the rock glacier system (about $5.351 \times 10^5 \text{ m}^2$), we can calculate a mean rate of erosion of the headwalls of between 1.0 and 2.5 mm/a. These results agree with estimates of erosion rate (~1.2-4.1 mm/a) from the granodioritic headwall of Bleis Marscha rock glacier in the eastern part of the Swiss Alps (Amschwand et al. 2021a). The catchment-wide denudation rate of the Ecrins-Pelvoux massif has been estimated to range from around 0.3 to 1.1 mm/a on millennial timescales using ^{10}Be concentrations in stream sediment (Delunel et al., 2010), suggesting that frost-cracking processes strongly control the post-glacial topographic evolution of mid-latitude mountain belts. The high erosion rates estimated in our study highlight that the steep rock walls that serve as the sources for debris on the rock glacier are retreating rapidly. This may be aided by the downstream conveyance of boulders/debris by the rock glaciers that prevent the headwalls from burying themselves in their own debris. This system therefore promotes the maintenance of high rockwall erosion rates, the development of cirques, and the possibility of distinctly asymmetric mountain ridges where the local climate is more conducive to rock glacier development on one side of a ridge than the other (Gilbert, 1904).

605 Conclusion

In this study, we quantitatively constrain the surface displacement field of an alpine rock glacier system over Holocene and modern timescales, by using both remote-sensing and geochronological datasets. The ^{10}Be surface-exposure dating of individual boulders along the main center line of the rock glacier reveals ages from 13.1 to 1.8 ka, corresponding to elevations of 2535 and 2751 m a.s.l., respectively. Our first-order observation shows an inverse correlation between ^{10}Be surface-exposure age and elevation, as well as a positive correlation between ^{10}Be surface-exposure age and distance from the headwall. This confirms the simple conceptual model in which rock debris falls from the headwall and remains at the surface as they are transported down valley by the rock glacier. Comparison of replicates from the transverse ridges along the rock glacier shows that loss/incomplete exposure due to surface erosion, burial or tilting of the boulders is negligible.

615 These replicates also show that ^{10}Be concentrations of boulders close to the headwall can vary, which in turn provides constraint on the inheritance/pre-exposure of rock boulders. We estimate the possible maximum inheritance of 2.16 ka in our study area, corresponding to the residence time of boulders in the headwall.

620 Comparison of orthoimages from both aerial (1960) and satellite (2018) surveys shows that the rock glacier system is composed of two uppermost active units with surface velocity of about 0.14 m/a at elevations from 2867 and 2626 m a.s.l., and a transitional unit with surface velocity of about 0.03 m/a at elevations between 2685 and 2556 m a.s.l. Analysis of a stable area outboard of the rock glacier system constrains the detection limit to be 0.02 m/a. Reported values of less than this detection threshold imply that the downstream part of the rock glacier, below 2600 m a.s.l. is presently immobile, confirming our geomorphic analysis of the feature as relict. The comparison of the surface velocities estimated using the ^{10}Be surface-exposure dating relative to distance to the headwall, and from the surface displacement integrated over the 1960-2018 period between the orthoimage surveys, shows that late Holocene and modern velocities are comparable on the active units of the rock glacier system.

630 Comparison of these results for the entire rock glacier allows us to propose an activity history for the Vallon de la Route rock glacier that consists of two main phases of surface displacement. The first episode lasted between about 12.1 ka and 6.26 ± 1.96 ka, with onset around the end of the Younger Dryas cooling event, when the cirques became ice free, allowing the headwall and scree field to feed the rock glacier with debris, with insulation of the ice beneath. After a period of quiescence, the second phase of activity started around 3.4 ka and continues towards the present, possibly attributed to the more favourable climate of the Neoglacial/Little Ice Age periods. Finally, we use the surface velocities obtained using ^{10}Be surface-exposure dating to reconstruct the erosion rate of the headwalls. The suggested erosion rates are between 1.0 and 2.5 mm/a. These are higher than catchment-wide denudation rates estimated over millennial timescales over the entire Ecrins-Pelvoux massif, suggesting that the rock glacier system promotes the maintenance of high rock wall erosion (back-wearing) rates and the development of cirques. To go further in reconstructing the paleo-environmental conditions of this specific region, physically based numerical modeling of rock glacier evolution (e.g., Anderson et al., 2018) should be applied using the existing topography, the spatial patterns of ^{10}Be surface-exposure ages and the modern surface velocities as modeling targets.

640 **Author contribution**

BL and RSA designed the study. BL and XB chose the study site and collected the samples in the field. PGV and JC supervised the TCN lab work of BL and provides the financial support for the TCN dating. BL and DC performed the remote-sensing analysis. BL and RSA wrote the numerical modelling experiments. All authors contributed to the writing of the manuscript.

645

Competing interest

The authors declare that they have no conflict of interest.

Acknowledgements

650 This study has been funded through the Mobility fellowship P2LAP2_191400 of the Swiss National Science Foundation. The authors acknowledge the Joseph Fourier alpine station for providing logistical and hosting support during the field campaign and the ASTER team (K. Keddadouche, G. Aumaitre, R. Braucher and V. Godard) for AMS analyses. The TRB team (ISTerre) is acknowledged for providing financial support for TCN dating. P.G.V. acknowledges funding from the Swiss National Science Foundation SNSF (Grant 639 PP00P2_170559) and the French ANR-PIA programme (ANR-18-655 MPGA-0006).

References

- Amschwand, Dominik, Susan Ivy-Ochs, Marcel Frehner, Olivia Steinemann, Marcus Christl, and Christof Vockenhuber. 2021a. “Deciphering the Evolution of the Bleis Marscha Rock Glacier (Val d’Err, Eastern Switzerland) with Cosmogenic Nuclide Exposure Dating, Aerial Image Correlation, and Finite Element Modeling.” *Cryosphere* 15 (4): 2057–81. <https://doi.org/10.5194/tc-15-2057-2021>.
- 660 Anderson, Robert S., Leif S. Anderson, William H. Armstrong, Matthew W. Rossi, and Sarah E. Crump. 2018. “Glaciation of Alpine Valleys: The Glacier – Debris-Covered Glacier – Rock Glacier Continuum.” *Geomorphology* 311: 127–42. <https://doi.org/10.1016/j.geomorph.2018.03.015>.
- Andrés, Nuria, Antonio Gómez-Ortiz, José M. Fernández-Fernández, Luis M. Tanarro, Ferran Salvador-Franch, Marc Oliva, and David Palacios. 2018. “Timing of Deglaciation and Rock Glacier Origin in the Southeastern Pyrenees: A Review and New Data.” *Boreas* 47 (4): 1050–71. <https://doi.org/10.1111/bor.12324>.
- 665 Balco, Greg, John O. Stone, Nathaniel A. Lifton, and Tibor J. Dunai. 2008. “A Complete and Easily Accessible Means of Calculating Surface Exposure Ages or Erosion Rates from ^{10}Be and ^{26}Al Measurements.” *Quaternary Geochronology* 3 (3): 174–95. <https://doi.org/10.1016/j.quageo.2007.12.001>.
- 670 Barboux, Chloé, Reynald Delaloye, and Christophe Lambiel. 2014. “Inventorying Slope Movements in an Alpine Environment Using DInSAR.” *Earth Surface Processes and Landforms* 39 (15): 2087–99. <https://doi.org/10.1002/esp.3603>.
- Barsch, Dietrich. 1977. “nature and importance of mass-wasting by rock glaciers in alpine permafrost environments.” *Earth Surf Process* 2 (2–3): 231–45. <https://doi.org/10.1002/esp.3290020213>.
- 675 Berthling, Ivar. 2011. “Beyond Confusion: Rock Glaciers as Cryo-Conditioned Landforms.” *Geomorphology* 131 (3–4): 98–106. <https://doi.org/10.1016/j.geomorph.2011.05.002>.
- Blöthe, Jan Henrik, Christian Halla, Ellen Schwalbe, Estefania Bottegal, Dario Trombotto Liaudat, and Lothar Schrott. 2021. “Surface Velocity Fields of Active Rock Glaciers and Ice-debris Complexes in the Central Andes of Argentina.” *Earth Surface Processes and Landforms* 46 (2): 504–22. <https://doi.org/10.1002/esp.5042>.

- 680 Bodin, Xavier. 2013. "Present Status and Development of Rock Glacier Complexes in South-Faced Valleys (45°N, French Alps)." *Geografia Fisica e Dinamica Quaternaria* 36 (1): 27–38. <https://doi.org/10.4461/GFDQ.2013.36.2>.
- Bodin, Xavier, Emmanuel Thibert, Olivier Sanchez, Antoine Rabatel, and Stéphane Jaillet. 2018. "Multi-Annual Kinematics of an Active Rock Glacier Quantified from Very High-Resolution DEMs: An Application-Case in the French Alps." *Remote Sensing* 10 (4). <https://doi.org/10.3390/rs10040547>.
- 685 Böhlert, Ralph, Michael Compeer, Markus Egli, Dagmar Brandová, Max Maisch, Peter W. Kubik, and Wilfried Haeberli. 2011. "A Combination of Relative-Numerical Dating Methods Indicates Two High Alpine Rock Glacier Activity Phases after the Glacier Advance of the Younger Dryas." *Open Geography Journal* 4: 115–30. <https://doi.org/10.2174/1874923201104010115>.
- Braucher R., D. Bourlès, S. Merchel, J. Vidal Romani, D. Fernandez-Mosquera, K. Marti, L. Léanni, F. Chauvet, M. Arnold, 690 G. Aumaître, K. Keddadouche, Determination of muon attenuation lengths in depth profiles from in situ produced cosmogenic nuclides, Nuclear Instruments and Methods in Physics Research Section B: Beam Interactions with Materials and Atoms, Volume 294, 2013, Pages 484-490, ISSN 0168-583X, <https://doi.org/10.1016/j.nimb.2012.05.023>.
- Brown, Erik Thorson, John M. Edmond, Grant M. Raisbeck, Françoise Yiou, Mark D. Kurz, and Edward J. Brook. 1991. 695 "Examination of Surface Exposure Ages of Antarctic Moraines Using in Situ Produced ¹⁰Be and ²⁶Al." *Geochimica et Cosmochimica Acta* 55 (8): 2269–83. [https://doi.org/10.1016/0016-7037\(91\)90103-C](https://doi.org/10.1016/0016-7037(91)90103-C).
- Charton, Joanna, Deborah Verfaillie, Vincent Jomelli, and Bernard Francou. 2021. "Early Holocene Rock Glacier Stabilisation at Col Du Lautaret (French Alps): Palaeoclimatic Implications." *Geomorphology* 394. <https://doi.org/10.1016/j.geomorph.2021.107962>.
- 700 Chenet, Marie, Daniel Brunstein, Vincent Jomelli, Erwan Roussel, Vincent Rinterknecht, Fatima Mokadem, Melody Biette, Vincent Robert, and Laëtitia Léanni. 2016. "¹⁰Be Cosmic-Ray Exposure Dating of Moraines and Rock Avalanches in the Upper Romanche Valley (French Alps): Evidence of Two Glacial Advances during the Late Glacial/Holocene Transition." *Quaternary Science Reviews* 148: 209–21. <https://doi.org/10.1016/j.quascirev.2016.07.025>.
- Claude, Anne, Susan Ivy-Ochs, Florian Kober, Marco Antognini, Bernhard Salcher, and Peter W. Kubik. 2014. "The 705 Chironico Landslide (Valle Leventina, Southern Swiss Alps): Age and Evolution." *Swiss Journal of Geosciences* 107 (2–3): 273–91. <https://doi.org/10.1007/s00015-014-0170-z>.
- Cossart, Etienne, Monique Fort, Didier Bourles, Julien Carcaillet, Romain Perrier, Lionel Siame, and Régis Braucher. 2010. "Climatic Significance of Glacier Retreat and Rockglaciers Re-Assessed in the Light of Cosmogenic Dating and Weathering Rind Thickness in Clarée Valley (Briançonnais, French Alps)." *Catena* 80 (3): 204–19. 710 <https://doi.org/10.1016/j.catena.2009.11.007>.
- Coûteaux, Michel, and Jean-Louis Edouard. 1987. "La Déglaçiation Du Site Du Lac Des Bèches (Massif Des Ecrins). Etude Pollenanalytique et Glacio-Morphologique." *Revue de Géographie Alpine* 75 (1): 63–77. <https://doi.org/10.3406/rga.1987.2666>.

- Cusicanqui, Diego, Antoine Rabatel, and Christian Vincent. 2021. "Interpretation of Volume and Flux Changes of the Laurichard Rock Glacier Between 1952 and 2019, French Alps." *Journal of Geophysical Research: Earth Surface*. <https://doi.org/10.1029/2021JF006161>.
715
- Dall'Asta, Elisa, Gianfranco Forlani, Riccardo Roncella, Marina Santise, Fabrizio Diotri, and Umberto Morra di Cella. 2017. "Unmanned Aerial Systems and DSM Matching for Rock Glacier Monitoring." *ISPRS Journal of Photogrammetry and Remote Sensing* 127 (May): 102–14. <https://doi.org/10.1016/j.isprsjprs.2016.10.003>.
- 720 Delaloye, Reynald, and Thomas Echelard. 2020. "IPA Action Group Rock Glacier Inventories and Kinematics (Version 4.1)." *International Permafrost Association*, 1–13.
- Delaloye, Reynald, Christophe Lambiel, and Isabelle Gärtner-Roer. 2010. "Aperçu de La Cinématique Des Glaciers Rocheux Dans Les Alpes Suisses. Rythme Saisonnier, Variations Interannuelles et Tendances Pluri-Décennales." *Geographica Helvetica* 65 (2): 135–45. <https://doi.org/10.5194/gh-65-135-2010>.
- 725 Delunel, R. 2010. "Evolution Géomorphologique Du Massif Des Ecrins-Pelvoux Depuis Le Dernier Maximum Glaciaire – Apports Des Nucléides Cosmogéniques Produits in-Situ." *Université Joseph Fourier (Grenoble, France)* Ph. D. Thesis: 236pp.
- Delunel, Romain, Peter A. van der Beek, Julien Carcaillet, Didier L. Bourlès, and Pierre G. Valla. 2010. "Frost-Cracking Control on Catchment Denudation Rates: Insights from in Situ Produced ¹⁰Be Concentrations in Stream Sediments (Ecrins-Pelvoux Massif, French Western Alps)." *Earth and Planetary Science Letters* 293 (1–2): 72–83. <https://doi.org/10.1016/j.epsl.2010.02.020>.
- 730 Delunel, Romain, Didier L. Bourlès, Peter A. van der Beek, Fritz Schlunegger, Ingo Leya, Jozef Masarik, and Emmanuel Paquet. 2014. "Snow Shielding Factors for Cosmogenic Nuclide Dating Inferred from Long-Term Neutron Detector Monitoring." *Quaternary Geochronology* 24: 16–26. <https://doi.org/10.1016/j.quageo.2014.07.003>.
- 735 Eriksen, H., L. Rouyet, T. R. Lauknes, I. Berthling, K. Isaksen, H. Hindberg, Y. Larsen, and G. D. Corner. 2018. "Recent Acceleration of a Rock Glacier Complex, Ádjet, Norway, Documented by 62 Years of Remote Sensing Observations." *Geophysical Research Letters* 45 (16): 8314–23. <https://doi.org/10.1029/2018GL077605>.
- Federici, Paolo Roberto, Darryl E. Granger, Marta Pappalardo, Adriano Ribolino, Matteo Spagnolo, and Andrew J. Cyr. 2008. "Exposure Age Dating and Equilibrium Line Altitude Reconstruction of an Egesen Moraine in the Maritime Alps, Italy." *Boreas* 37 (2): 245–53. <https://doi.org/10.1111/j.1502-3885.2007.00018.x>.
- 740 Fernández-Fernández, José M., David Palacios, Nuria Andrés, Irene Schimmelpfennig, Luis M. Tanarro, Skafti Brynjólfsson, Francisco J. López-Acevedo, Þorsteinn Sæmundsson, and A.S.T.E.R. Team. 2020. "Constraints on the Timing of Debris-Covered and Rock Glaciers: An Exploratory Case Study in the Hólar Area, Northern Iceland." *Geomorphology* 361: 107196. <https://doi.org/10.1016/j.geomorph.2020.107196>.
- 745 Fleischer, Fabian, Florian Haas, Livia Piermattei, Madlene Pfeiffer, Tobias Heckmann, Moritz Altmann, Jakob Rom, et al. n.d. "Multi-Decadal (1953–2017) Rock Glacier Kinematics Analysed by High-Resolution Topographic Data in the

- Upper Kaunertal, Austria.” *Tc.Copernicus.Org*. Accessed March 24, 2022. <https://tc.copernicus.org/preprints/tc-2021-77/>.
- 750 Francou, Bernard. 1982. “Chutes de Pierres et Éboulisation Dans Les Parois de l’étage Périglaciaire.” *Revue de Géographie Alpine* 70 (3): 279–300. <https://doi.org/10.3406/rga.1982.2508>.
- Francou, Bernard, and Louis Reynaud. 1992. “10 Year Surficial Velocities on a Rock Glacier (Laurichard, French Alps).” *Permafrost and Periglacial Processes* 3 (3): 209–13. <https://doi.org/10.1002/ppp.3430030306>.
- Frauenfelder, R., and A. Kááb. 2000. “Towards a Palaeoclimatic Model of Rock Glacier Formation in the Swiss Alps.” *Annals of Glaciology* 31: 281–86. <https://doi.org/10.3189/172756400781820264>.
- 755 Frehner, Marcel, Anna Hui Mee Ling, and Isabelle Gärtner-Roer. 2015. “Furrow-and-Ridge Morphology on Rockglaciers Explained by Gravity-Driven Buckle Folding: A Case Study from the Murtèl Rockglacier (Switzerland).” *Permafrost and Periglacial Processes* 26 (1): 57–66. <https://doi.org/10.1002/ppp.1831>.
- Fuchs, Margret C., Ralph Böhlert, Matthias Krbetschek, Frank Preusser, and Markus Egli. 2013. “Exploring the Potential of Luminescence Methods for Dating Alpine Rock Glaciers.” *Quaternary Geochronology* 18: 17–33. <https://doi.org/10.1016/j.quageo.2013.07.001>.
- 760 Gallach, Xavi, Julien Carcaillet, Ludovic Ravel, Philip Deline, Christophe Ogier, Magali Rossi, Emmanuel Malet, and David Garcia-Sellés. 2020. “Climatic and Structural Controls on Late-glacial and Holocene Rockfall Occurrence in High-elevated Rock Walls of the Mont Blanc Massif (Western Alps).” *Earth Surface Processes and Landforms* 45 (13): 3071–91. <https://doi.org/10.1002/esp.4952>.
- 765 Gallach, Xavi, Ludovic Ravel, Markus Egli, Dagmar Brandova, Michael Schaepman, Marcus Christl, Stephan Gruber, Philip Deline, Julien Carcaillet, and François Pallandre. 2018. “Timing of Rockfalls in the Mont Blanc Massif (Western Alps): Evidence from Surface Exposure Dating with Cosmogenic ¹⁰Be.” *Landslides* 15 (10): 1991–2000. <https://doi.org/10.1007/s10346-018-0999-8>.
- García-Ruiz, JM, D. Palacios, JM Fernández-Fernández, N. Andrés, J. Arnáez, A. Gómez-Villar, J. Santos-González, J. 770 Álvarez-Martínez, N. Lana-Renault, L. Léanni, Glacial stages in the Peña Negra valley, Iberian Range, northern Iberian Peninsula: Assessing the importance of the glacial record in small cirques in a marginal mountain area, *Geomorphology*, Volume 362, 2020, 107195, ISSN 0169-555X, <https://doi.org/10.1016/j.geomorph.2020.107195>.
- Gardent, Marie, Antoine Rabatel, Jean Pierre Dedieu, and Philip Deline. 2014. “Multitemporal Glacier Inventory of the French Alps from the Late 1960s to the Late 2000s.” *Global and Planetary Change* 120: 24–37. <https://doi.org/10.1016/j.gloplacha.2014.05.004>.
- 775 Giardino, John R., and John D. Vitek. 1988. “The Significance of Rock Glaciers in the Glacial-periglacial Landscape Continuum.” *Journal of Quaternary Science* 3 (1): 97–103. <https://doi.org/10.1002/jqs.3390030111>.
- Gilbert, G. K. 1904. “Systematic Asymmetry of Crest Lines in the High Sierra of California.” *The Journal of Geology* 12 (7): 579–88. <https://doi.org/10.1086/621182>.

- 780 Gosse, John C., and Fred M. Phillips. 2001. "Terrestrial in Situ Cosmogenic Nuclides: Theory and Application." *Quaternary Science Reviews* 20 (14): 1475–1560. [https://doi.org/10.1016/S0277-3791\(00\)00171-2](https://doi.org/10.1016/S0277-3791(00)00171-2).
- Haeberli, Wilfried. 2013. "Mountain Permafrost - Research Frontiers and a Special Long-Term Challenge." *Cold Regions Science and Technology* 96 (December): 71–76. <https://doi.org/10.1016/j.coldregions.2013.02.004>.
- Haeberli, Wilfried, Bernard Hallet, Lukas Arenson, Roger Elconin, Ole Humlum, Andreas Kääh, Viktor Kaufmann, et al.
785 2006. "Permafrost Creep and Rock Glacier Dynamics." *Permafrost and Periglacial Processes* 17 (3): 189–214. <https://doi.org/10.1002/ppp.561>.
- Hippolyte, Jean Claude, Didier Bourlès, Régis Braucher, Julien Carcaillet, Laëtitia Léanni, Maurice Arnold, and Georges Aumaitre. 2009. "Cosmogenic ^{10}Be Dating of a Sackung and Its Faulted Rock Glaciers, in the Alps of Savoy (France)." *Geomorphology* 108 (3–4): 312–20. <https://doi.org/10.1016/j.geomorph.2009.02.024>.
- 790 Hofmann, Felix Martin, Helena Alexanderson, Philippe Schoeneich, Jordan R. Mertes, and Laëtitia Léanni. 2019. "Post-Last Glacial Maximum Glacier Fluctuations in the Southern Écrins Massif (Westernmost Alps): Insights from ^{10}Be Cosmic Ray Exposure Dating." *Boreas* 48 (4): 1019–41. <https://doi.org/10.1111/BOR.12405>.
- Hormes, Anne, Susan Ivy-Ochs, Peter W. Kubik, Luca Ferreli, and Alessandro Maria Michetti. 2008. " ^{10}Be Exposure Ages of a Rock Avalanche and a Late Glacial Moraine in Alta Valtellina, Italian Alps." *Quaternary International* 190 (1):
795 136–45. <https://doi.org/10.1016/j.quaint.2007.06.036>.
- Humlum, Ole. 2000. "The Geomorphic Significance of Rock Glaciers: Estimates of Rock Glacier Debris Volumes and Headwall Recession Rates in West Greenland." *Geomorphology* 35 (1–2): 41–67. [https://doi.org/10.1016/S0169-555X\(00\)00022-2](https://doi.org/10.1016/S0169-555X(00)00022-2).
- Ikeda, Atsushi, and Norikazu Matsuoka. 2006. "Pebbly versus Bouldery Rock Glaciers: Morphology, Structure and
800 Processes." *Geomorphology* 73 (3–4): 279–96. <https://doi.org/10.1016/j.geomorph.2005.07.015>.
- Ikeda, Atsushi, Norikazu Matsuoka, and Andreas Kääh. 2008. "Fast Deformation of Perennially Frozen Debris in a Warm Rock Glacier in the Swiss Alps: An Effect of Liquid Water." *Journal of Geophysical Research: Earth Surface* 113 (1). <https://doi.org/10.1029/2007JF000859>.
- Ivy-Ochs, S. 2015. "Variaciones Glaciares En Los Alphas Europeos al Final de La Última Glaciación." *Cuadernos de
805 Investigacion Geografica* 41 (2): 295–315. <https://doi.org/10.18172/cig.2750>.
- Ivy-Ochs, Susan, Hanns Kerschner, Peter W. Kubik, and Christian Schlüchter. 2006. "Glacier Response in the European Alps to Heinrich Event 1 Cooling: The Gschnitz Stadial." *Journal of Quaternary Science*. <https://doi.org/10.1002/jqs.955>.
- Ivy-Ochs, Susan, Hanns Kerschner, Anne Reuther, Frank Preusser, Klaus Heine, Max Maisch, Peter W. Kubik, and
810 Christian Schlüchter. 2008. "Chronology of the Last Glacial Cycle in the European Alps." *Journal of Quaternary Science* 23 (6–7): 559–73. <https://doi.org/10.1002/jqs.1202>.
- Johnson, P. G. 1980. "Glacier- Rock Glacier Transition in the Southwest Yukon Territory, Canada." *Arctic and Alpine Research* 12 (2): 195–204. <https://doi.org/10.2307/1550516>.

- Jones, Darren B., Stephan Harrison, Karen Anderson, and W. Brian Whalley. 2019. "Rock Glaciers and Mountain Hydrology: A Review." *Earth-Science Reviews* 193 (March): 66–90. <https://doi.org/10.1016/j.earscirev.2019.04.001>.
- 815 Kaab, A., W. Haeberli, and G. Hilmar Gudmundsson. 1997. "Analysing the Creep of Mountain Permafrost Using High Precision Aerial Photogrammetry: 25 Years of Monitoring Gruben Rock Glacier, Swiss Alps." *Permafrost and Periglacial Processes* 8 (4): 409–26. [https://doi.org/10.1002/\(SICI\)1099-1530\(199710/12\)8:4<409::AID-PPP267>3.0.CO;2-C](https://doi.org/10.1002/(SICI)1099-1530(199710/12)8:4<409::AID-PPP267>3.0.CO;2-C).
- 820 Kääh, Andreas, Tazio Strozzi, Tobias Bolch, Rafael Caduff, H. Kon Trefall, Markus Stoffel, and Alexander Kokarev. 2021. "Inventory and Changes of Rock Glacier Creep Speeds in Ile Alatau and Kungöy Ala-Too, Northern Tien Shan, since the 1950s." *Cryosphere* 15 (2): 927–49. <https://doi.org/10.5194/tc-15-927-2021>.
- Kellerer-Pirklbauer, Andreas. 2017. "Potential Weathering by Freeze-Thaw Action in Alpine Rocks in the European Alps during a Nine Year Monitoring Period." *Geomorphology* 296: 113–31. <https://doi.org/10.1016/j.geomorph.2017.08.020>.
- 825 Kellerer-Pirklbauer, Andreas, and Matthias Rieckh. 2016. "Monitoring Nourishment Processes in the Rooting Zone of an Active Rock Glacier in an Alpine Environment." *Zeitschrift Fur Geomorphologie* 60 (August): 99–121. https://doi.org/10.1127/zfg_suppl/2016/00245.
- Kelly, Meredith A., Jean François Buoncristiani, and Christian Schlüchter. 2004. "A Reconstruction of the Last Glacial Maximum (LGM) Ice-Surface Geometry in the Western Swiss Alps and Contiguous Alpine Regions in Italy and France." *Eclogae Geologicae Helvetiae* 97 (1): 57–75. <https://doi.org/10.1007/s00015-004-1109-6>.
- 830 Kenner, Robert, Marcia Phillips, Philippe Limpach, Jan Beutel, and Martin Hiller. 2018. "Monitoring Mass Movements Using Georeferenced Time-Lapse Photography: Ritigraben Rock Glacier, Western Swiss Alps." *Cold Regions Science and Technology* 145 (January): 127–34. <https://doi.org/10.1016/j.coldregions.2017.10.018>.
- 835 Kohl, C. P., and K. Nishiizumi. 1992. "Chemical Isolation of Quartz for Measurement of In-Situ -Produced Cosmogenic Nuclides." *Geochimica et Cosmochimica Acta*. Pergamon. [https://doi.org/10.1016/0016-7037\(92\)90401-4](https://doi.org/10.1016/0016-7037(92)90401-4).
- Krainer, Karl, David Bressan, Benjamin Dietre, Jean Nicolas Haas, Irka Hajdas, Kathrin Lang, Volkmar Mair, et al. 2015. "A 10,300-Year-Old Permafrost Core from the Active Rock Glacier Lazaun, Southern Ötztal Alps (South Tyrol, Northern Italy)." *Quaternary Research (United States)* 83 (2): 324–35. <https://doi.org/10.1016/j.yqres.2014.12.005>.
- 840 Lifton, Nathaniel, Tatsuhiko Sato, and Tibor J. Dunai. 2014. "Scaling in Situ Cosmogenic Nuclide Production Rates Using Analytical Approximations to Atmospheric Cosmic-Ray Fluxes." *Earth and Planetary Science Letters* 386 (January): 149–60. <https://doi.org/10.1016/j.epsl.2013.10.052>.
- Liu, L., C. I. Millar, R. D. Westfall, and H. A. Zebker. 2013. "Surface Motion of Active Rock Glaciers in the Sierra Nevada, California, USA: Inventory and a Case Study Using InSAR." *Cryosphere* 7 (4): 1109–19. <https://doi.org/10.5194/tc-7-1109-2013>.
- 845 Liu, Zhengyu, Jiang Zhu, Yair Rosenthal, Xu Zhang, Bette L. Otto-Bliesner, Axel Timmermann, Robin S. Smith, Gerrit Lohmann, Weipeng Zheng, and Oliver Elison Timm. 2014. "The Holocene Temperature Conundrum." *Proceedings of*

the National Academy of Sciences of the United States of America 111 (34): E3501.
<https://doi.org/10.1073/PNAS.1407229111/-/DCSUPPLEMENTAL>.

- 850 Marcer, Marco, Xavier Bodin, Alexander Brenning, Philippe Schoeneich, Raphaële Charvet, and Frédéric Gottardi. 2017. “Permafrost Favorability Index: Spatial Modeling in the French Alps Using a Rock Glacier Inventory.” *Frontiers in Earth Science* 5 (December). <https://doi.org/10.3389/feart.2017.00105>.
- Marcer, Marco, Alessandro Cicoira, Diego Cusicanqui, Xavier Bodin, Thomas Echelard, Renée Obregon, and Philippe Schoeneich. 2021. “Rock Glaciers throughout the French Alps Accelerated and Destabilised since 1990 as Air
855 Temperatures Increased.” *Communications Earth & Environment* 2 (1): 1–11. <https://doi.org/10.1038/s43247-021-00150-6>.
- Martin, L. C.P., P. H. Blard, G. Balco, J. Lavé, R. Delunel, N. Lifton, and V. Laurent. 2017. “The CREp Program and the ICE-D Production Rate Calibration Database: A Fully Parameterizable and Updated Online Tool to Compute Cosmic-Ray Exposure Ages.” *Quaternary Geochronology* 38: 25–49. <https://doi.org/10.1016/j.quageo.2016.11.006>.
- 860 Matthews, John A., and Peter Wilson. 2015. “Improved Schmidt-Hammer Exposure Ages for Active and Relict Pronival Ramparts in Southern Norway, and Their Palaeoenvironmental Implications.” *Geomorphology* 246: 7–21. <https://doi.org/10.1016/j.geomorph.2015.06.002>.
- Merchel, S., and U. Hergers. 1999. “An Update on Radiochemical Separation Techniques for the Determination of Long-Lived Radionuclides via Accelerator Mass Spectrometry.” *Radiochimica Acta* 84 (4): 215–19.
865 <https://doi.org/10.1524/ract.1999.84.4.215>.
- Micheletti, Natan, Marj Tonini, and Stuart N. Lane. 2017. “Geomorphological Activity at a Rock Glacier Front Detected with a 3D Density-Based Clustering Algorithm.” *Geomorphology* 278: 287–97. <https://doi.org/10.1016/j.geomorph.2016.11.016>.
- Monegato, Giovanni, Giancarlo Scardia, Irka Hajdas, Francesca Rizzini, and Andrea Piccin. 2017. “The Alpine LGM in the
870 Boreal Ice-Sheets Game.” *Scientific Reports* 7 (1): 1–8. <https://doi.org/10.1038/s41598-017-02148-7>.
- Monnier, Sébastien, and Christophe Kinnard. 2015. “Reconsidering the Glacier to Rock Glacier Transformation Problem: New Insights from the Central Andes of Chile.” *Geomorphology* 238 (June): 47–55. <https://doi.org/10.1016/j.geomorph.2015.02.025>.
- Moran, Andrew P., Susan Ivy-Ochs, Michael Schuh, Markus Christl, and Hanns Kerschner. 2016. “Evidence of Central
875 Alpine Glacier Advances during the Younger Dryas–Early Holocene Transition Period.” *Boreas* 45 (3): 398–410. <https://doi.org/10.1111/bor.12170>.
- Necsoiu, Marius, Alexandru Onaca, Sarah Wigginton, and Petru Urdea. 2016. “Rock Glacier Dynamics in Southern Carpathian Mountains from High-Resolution Optical and Multi-Temporal SAR Satellite Imagery.” *Remote Sensing of Environment* 177 (May): 21–36. <https://doi.org/10.1016/j.rse.2016.02.025>.
- 880 Nuth, C., and Kääb. 2011. “Co-Registration and Bias Corrections of Satellite Elevation Data Sets for Quantifying Glacier Thickness Change.” *Cryosphere* 5 (1): 271–90. <https://doi.org/10.5194/tc-5-271-2011>.

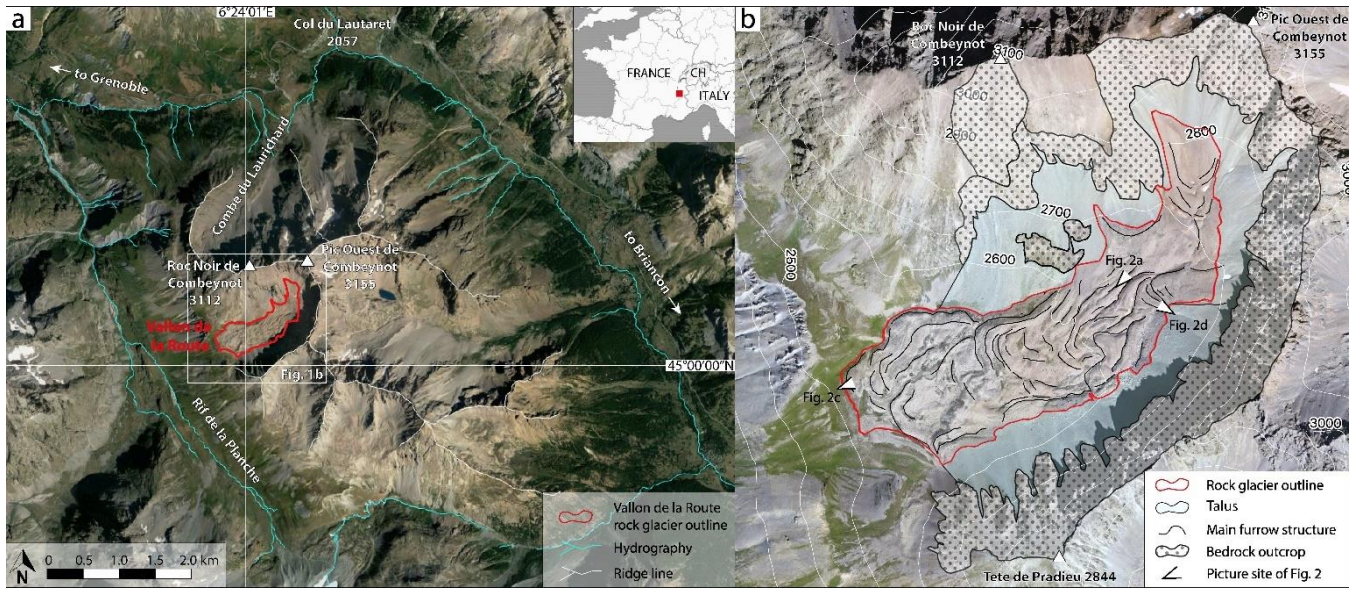
- Paasche, Øyvind, Svein Olaf Dahl, Reidar Løvlie, Jostein Bakke, and Atle Nesje. 2007. “Rockglacier Activity during the Last Glacial-Interglacial Transition and Holocene Spring Snowmelting.” *Quaternary Science Reviews* 26 (5–6): 793–807. <https://doi.org/10.1016/j.quascirev.2006.11.017>.
- 885 Palacios, David, Marc Oliva, Antonio Gómez-Ortiz, Nuria Andrés, José M. Fernández-Fernández, Irene Schimmelpfennig, Laëtitia Léanni, and A.S.T.E.R. Team. 2020. “Climate Sensitivity and Geomorphological Response of Cirque Glaciers from the Late Glacial to the Holocene, Sierra Nevada, Spain.” *Quaternary Science Reviews* 248 (November). <https://doi.org/10.1016/j.quascirev.2020.106617>.
- Pavón-Carrasco, Francisco Javier, María Luisa Osete, Joan Miquel Torta, and Angelo De Santis. 2014. “A Geomagnetic
890 Field Model for the Holocene Based on Archaeomagnetic and Lava Flow Data.” *Earth and Planetary Science Letters* 388 (February): 98–109. <https://doi.org/10.1016/j.epsl.2013.11.046>.
- Portenga, Eric W., and Paul R. Bierman. 2011. “Understanding Earth’s Eroding Surface with ^{10}Be .” *GSA Today* 21 (8): 4–10. <https://doi.org/10.1130/G111A.1>.
- Protin, M., I. Schimmelpfennig, Jean Louis Mugnier, Ludovic Ravanel, Melaine Le Roy, Philip Deline, Vincent Favier, et al.
895 2019. “Climatic Reconstruction for the Younger Dryas/Early Holocene Transition and the Little Ice Age Based on Paleo-Extents of Argentière Glacier (French Alps).” *Quaternary Science Reviews* 221 (October). <https://doi.org/10.1016/j.quascirev.2019.105863>.
- RGIK. 2020. “Rock Glacier Inventory Using InSAR (Kinematic Approach), Practical Guidelines v3.0.2.”
- Robson, Benjamin Aubrey, Tobias Bolch, Shelley MacDonell, Daniel Hölbling, Philipp Rastner, and Nicole Schaffer. 2020.
900 “Automated Detection of Rock Glaciers Using Deep Learning and Object-Based Image Analysis.” *Remote Sensing of Environment* 250 (December): 112033. <https://doi.org/10.1016/j.rse.2020.112033>.
- Robson, Benjamin Aubrey, Shelley MacDonell, Álvaro Ayala, Tobias Bolch, Pål Ringkjøb Nielsen, and Sebastián Vivero. 2022. “Glacier and Rock Glacier Changes since the 1950s in the La Laguna Catchment, Chile.” *The Cryosphere* 16 (2): 647–65. <https://doi.org/10.5194/TC-16-647-2022>.
- 905 Rodríguez-Rodríguez, Laura, Montserrat Jiménez-Sánchez, María José Domínguez-Cuesta, Vincent Rinterknecht, and Raimon Pallàs. 2017. “Timing of Last Deglaciation in the Cantabrian Mountains (Iberian Peninsula; North Atlantic Region) Based on in Situ-Produced ^{10}Be Exposure Dating.” *Quaternary Science Reviews* 171 (September): 166–81. <https://doi.org/10.1016/j.quascirev.2017.07.012>.
- Le Roy, Melaine, Philip Deline, Julien Carcaillet, Irene Schimmelpfennig, and Magali Ermini. 2017. “ ^{10}Be Exposure Dating
910 of the Timing of Neoglacial Glacier Advances in the Ecrins-Pelvoux Massif, Southern French Alps.” *Quaternary Science Reviews* 178 (December): 118–38. <https://doi.org/10.1016/j.quascirev.2017.10.010>.
- Sandeman, Alison F., and Colin K. Ballantyne. 1996. “Talus Rock Glaciers in Scotland: Characteristics and Controls on Formation.” *Scottish Geographical Magazine* 112 (3): 138–46. <https://doi.org/10.1080/14702549608554947>.

- Scambos, Theodore A., Melanie J. Dutkiewicz, Jeremy C. Wilson, and Robert A. Bindschadler. 1992. "Application of Image
915 Cross-Correlation to the Measurement of Glacier Velocity Using Satellite Image Data." *Remote Sensing of Environment* 42 (3): 177–86. [https://doi.org/10.1016/0034-4257\(92\)90101-O](https://doi.org/10.1016/0034-4257(92)90101-O).
- Scapozza, Cristian, Christophe Lambiel, Claudio Bozzini, Stefano Mari, and Marco Conedera. 2014. "Assessing the Rock
Glacier Kinematics on Three Different Timescales: A Case Study from the Southern Swiss Alps." *Earth Surface
Processes and Landforms* 39 (15): 2056–69. <https://doi.org/10.1002/esp.3599>.
- 920 Schimmelpfennig, Irene, Joerg M. Schaefer, Naki Akçar, Tobias Koffman, Susan Ivy-Ochs, Roseanne Schwartz, Robert C.
Finkel, Susan Zimmerman, and Christian Schlüchter. 2014. "A Chronology of Holocene and Little Ice Age Glacier
Culminations of the Steingletscher, Central Alps, Switzerland, Based on High-Sensitivity Beryllium-10 Moraine
Dating." *Earth and Planetary Science Letters* 393: 220–30. <https://doi.org/10.1016/j.epsl.2014.02.046>.
- Schindelwig, Inga, Naki Akçar, Peter W. Kubik, and Christian Schlüchter. 2012. "Lateglacial and Early Holocene Dynamics
925 of Adjacent Valley Glaciers in the Western Swiss Alps." *Journal of Quaternary Science* 27 (1): 114–24.
<https://doi.org/10.1002/jqs.1523>.
- Shean, David E., Oleg Alexandrov, Zachary M. Moratto, Benjamin E. Smith, Ian R. Joughin, Claire Porter, and Paul Morin.
2016. "An Automated, Open-Source Pipeline for Mass Production of Digital Elevation Models (DEMs) from Very-
High-Resolution Commercial Stereo Satellite Imagery." *ISPRS Journal of Photogrammetry and Remote Sensing* 116
930 (June): 101–17. <https://doi.org/10.1016/j.isprsjprs.2016.03.012>.
- Steinmann, Olivia, Jürgen M. Reitner, Susan Ivy-Ochs, Marcus Christl, and Hans Arno Synal. 2020. "Tracking Rockglacier
Evolution in the Eastern Alps from the Lateglacial to the Early Holocene." *Quaternary Science Reviews* 241 (August).
<https://doi.org/10.1016/j.quascirev.2020.106424>.
- Strozzi, Tazio, Rafael Caduff, Nina Jones, Chloé Barboux, Reynald Delaloye, Xavier Bodin, Andreas Kääh, Eva Mätzler,
935 and Lothar Schrott. 2020. "Monitoring Rock Glacier Kinematics with Satellite Synthetic Aperture Radar." *Remote
Sensing* 12 (3): 559. <https://doi.org/10.3390/rs12030559>.
- Thibert, Emmanuel, Xavier Bodin, Mylène Bonnefoy-Demongeot, and François Finance. 2018. "Extracting the Time Signal
in Surface Velocity Changes along 3 Decades at Laurichard Rock Glacier (French Alps)." In *5th European Conference
on Permafrost, Book of Abstract*. Presented at the EUCOP5, Laboratoire EDYTEM, Chamonix, France (pp. 615-616).
- 940 Uppala, S. M., P. W. Källberg, A. J. Simmons, U. Andrae, V. Da Costa Bechtold, M. Fiorino, J. K. Gibson, et al. 2005.
"The ERA-40 Re-Analysis." *Quarterly Journal of the Royal Meteorological Society* 131 (612): 2961–3012.
<https://doi.org/10.1256/qj.04.176>.
- Valla, Pierre G., Peter A. van der Beek, and Julien Carcaillet. 2010. "Dating Bedrock Gorge Incision in the French Western
945 Alps (Ecrins-Pelvoux Massif) Using Cosmogenic ¹⁰Be." *Terra Nova* 22 (1): 18–25. <https://doi.org/10.1111/j.1365-3121.2009.00911.x>.
- Vivero, Sebastián, Xavier Bodin, David Farías-Barahona, Shelley MacDonell, Nicole Schaffer, Benjamin Aubrey Robson,
and Christophe Lambiel. 2021. "Combination of Aerial, Satellite, and UAV Photogrammetry for Quantifying Rock

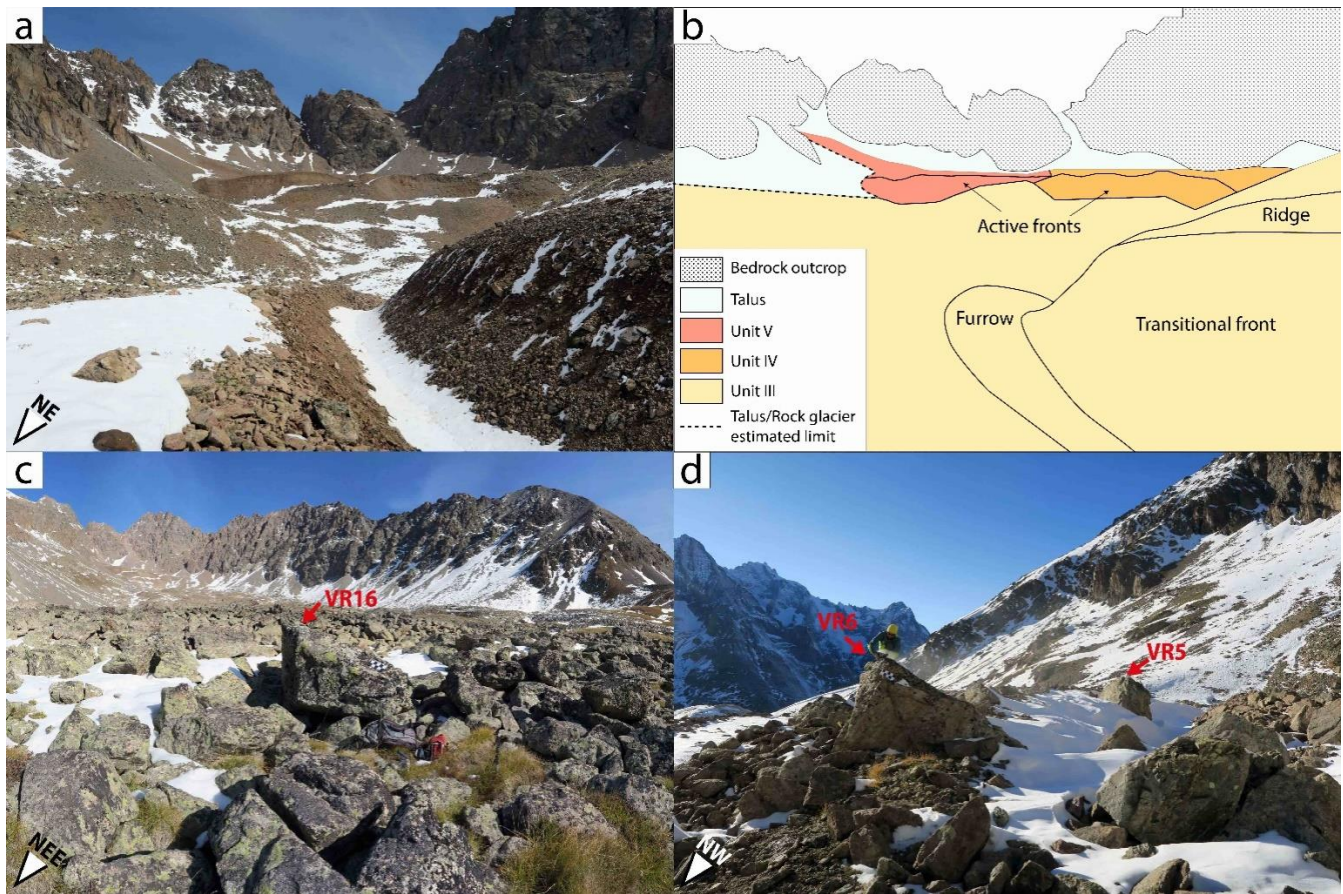
Glacier Kinematics in the Dry Andes of Chile (30°S) Since the 1950s.” *Frontiers in Remote Sensing* 2 (November).
<https://doi.org/10.3389/FRSEN.2021.784015/PDF>.

- 950 Vivero, Sebastián, and Christophe Lambiel. 2019. “Monitoring the Crisis of a Rock Glacier with Repeated UAV Surveys.”
Geographica Helvetica 74 (1): 59–69. <https://doi.org/10.5194/gh-74-59-2019>.
- Wahrhaftig, Clyde, and Allan Cox. 1959. “Rock Glaciers in the Alaska Range.” *Bulletin of the Geological Society of
America* 70 (4): 383–436. [https://doi.org/10.1130/0016-7606\(1959\)70\[383:RGITAR\]2.0.CO;2](https://doi.org/10.1130/0016-7606(1959)70[383:RGITAR]2.0.CO;2).
- Whalley, W. Brian. 1974. “Origin of Rock Glaciers.” *Journal of Glaciology* 13 (68): 323–24.
955 <https://doi.org/10.3189/s0022143000023145>.
- Winkler, Stefan, and Christophe Lambiel. 2018. “Age Constraints of Rock Glaciers in the Southern Alps/New Zealand –
Exploring Their Palaeoclimatic Potential.” *Holocene* 28 (5): 778–90. <https://doi.org/10.1177/0959683618756802>.
- Wirsig, Christian, Jerzy Zasadni, Susan Ivy-Ochs, Marcus Christl, Florian Kober, and Christian Schlüchter. 2016. “A
Deglaciation Model of the Oberhasli, Switzerland.” *Journal of Quaternary Science* 31 (1): 46–59.
960 <https://doi.org/10.1002/jqs.2831>.
- Wirz, V., S. Gruber, R. S. Purves, J. Beutel, I. Gärtner-Roer, S. Gubler, and A. Vieli. 2016. “Short-Term Velocity Variations
at Three Rock Glaciers and Their Relationship with Meteorological Conditions.” *Earth Surface Dynamics* 4 (1): 103–
23. <https://doi.org/10.5194/esurf-4-103-2016>.

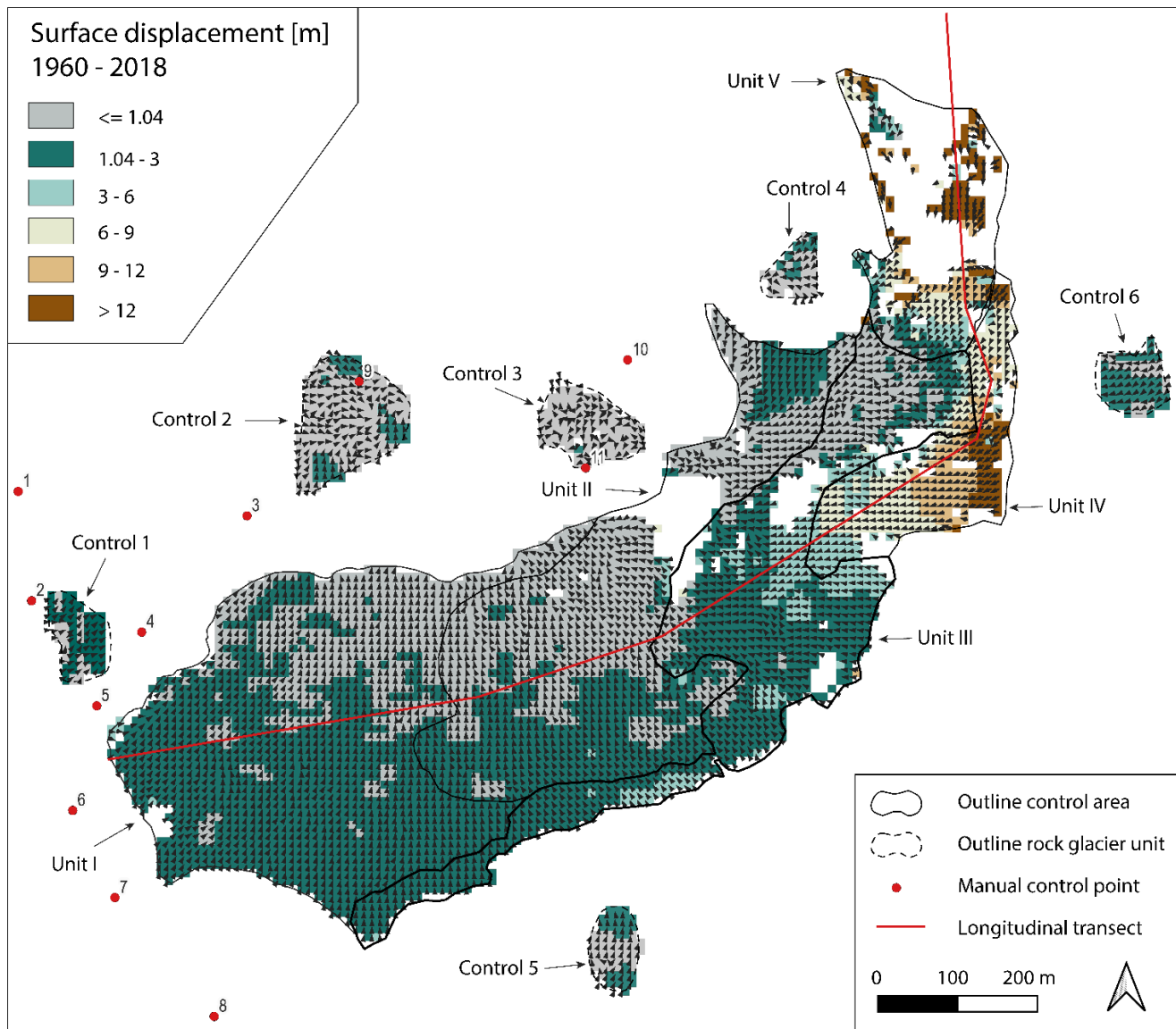
965



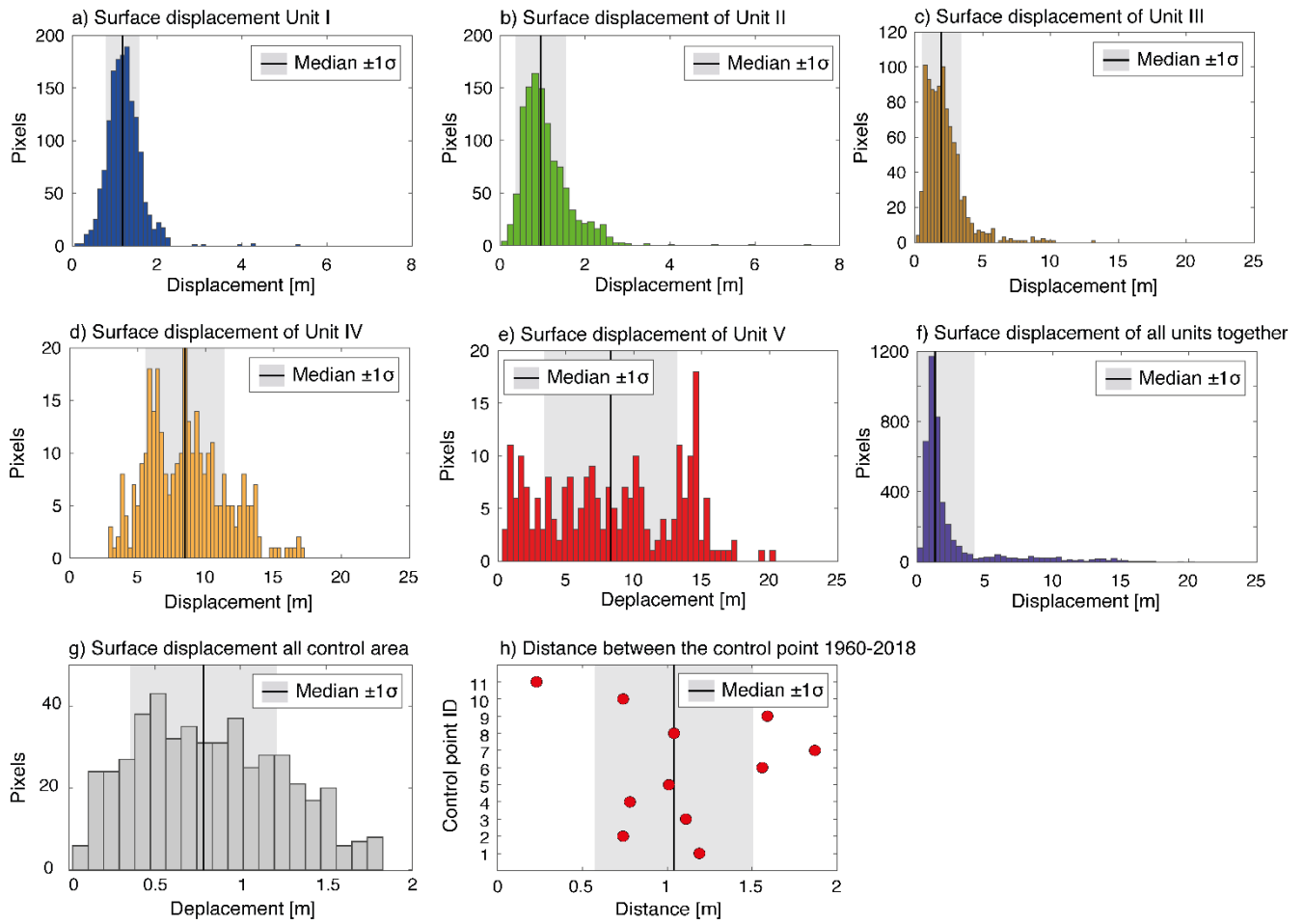
970 **Figure 1: a. Regional map of the Combeynot massif showing the Vallon de la Route rock glacier and surrounding topography (Satellite image from ©Google Earth 2020). Outline of the rock glacier (red), hydrography (cyan) and ridge line (white) from Bodin (2007). Inset shows location of the Vallon de la Route rock glacier within western Europe b. Map of the Vallon de la Route rock glacier, with outline of the rock glacier, main furrow structures, outline of the bedrock outcrops (from Bodin, 2007) and location/orientation of pictures presented in Figure 2. Satellite image from Bing Aerial ©Microsoft.**



975 **Figure 2:** a-b. Picture (a) looking toward the NE and geomorphological interpretation (b) of the rock glacier units III, IV and V, with bedrock outcrops, talus, ridge, furrow and fronts. c. Picture looking toward the NEE of the relict unit I and sampled boulder (VR16). d. Picture looking toward the NW of the ridge I where two different boulders were sampled (VR5 and VR6). Picture locations and orientations are indicated on Figure 1b.



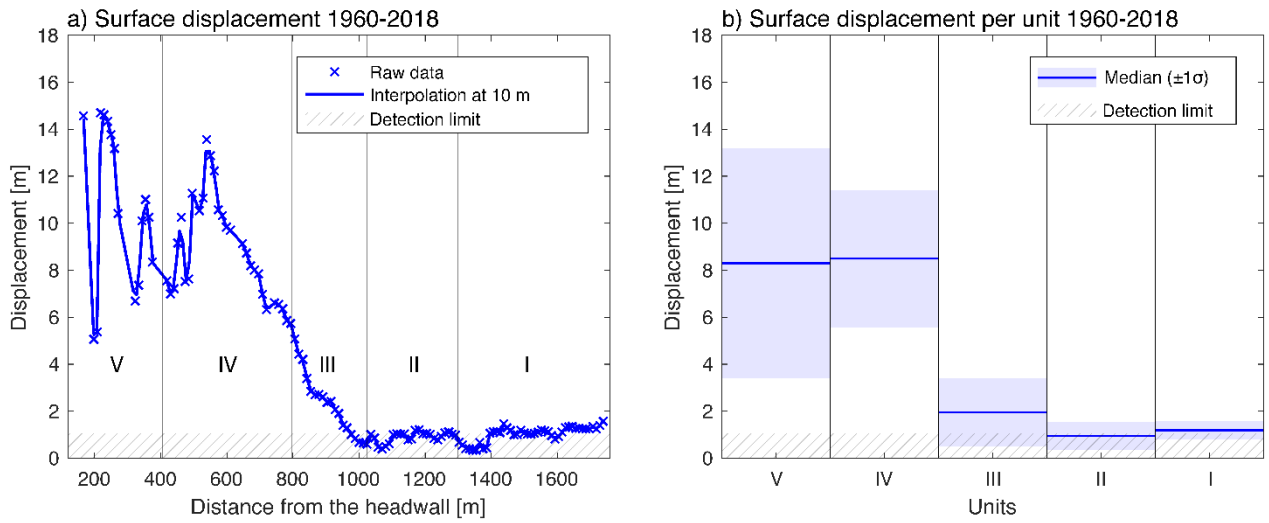
980 **Figure 3: Surface displacement map (1960-2018) of the Vallon de la Route rock glacier. Red line is the longitudinal transect used to extract surface displacement (Figure 5a). Black lines outline the different units of the rock glacier system. The dashed black line delimits the stable terrain control areas and red dots show the locations of the manual control points used to quantify uncertainties in the image correlation. Non-mapped area are the results of the filtering process as described in Section 3.1.3.**



985

Figure 4: a-f. Histograms of the surface displacements and median ($\pm 1\sigma$) values extracted for each unit are and the entire rock glacier. g. Histograms of the surface displacements and median ($\pm 1\sigma$) values extracted from the entire control areas as shown in Figures 3 and A1. Independent histograms of surface displacement values for each control area are presented in Figure A3. h. Distance between the two orthomosaics (1960 and 2018) manually estimated on control point (stable features) as shown in Figures 3 and A1 and Table 2.

990



995 **Figure 5: a. Surface displacement (1960-2018) extracted following the longitudinal transect (red line on Fig. 3) with identification of Units I to V. The blue line represents the 10-m interpolation of the raw data. b. Median surface displacement in each rock glacier unit with its $\pm 1\sigma$ variability (see Figure 4 for histograms). The cross-hatched pattern represents the detection limit defined by median value of the control areas (Figure 4) used as a threshold value for detection of rock glacier surface displacement.**

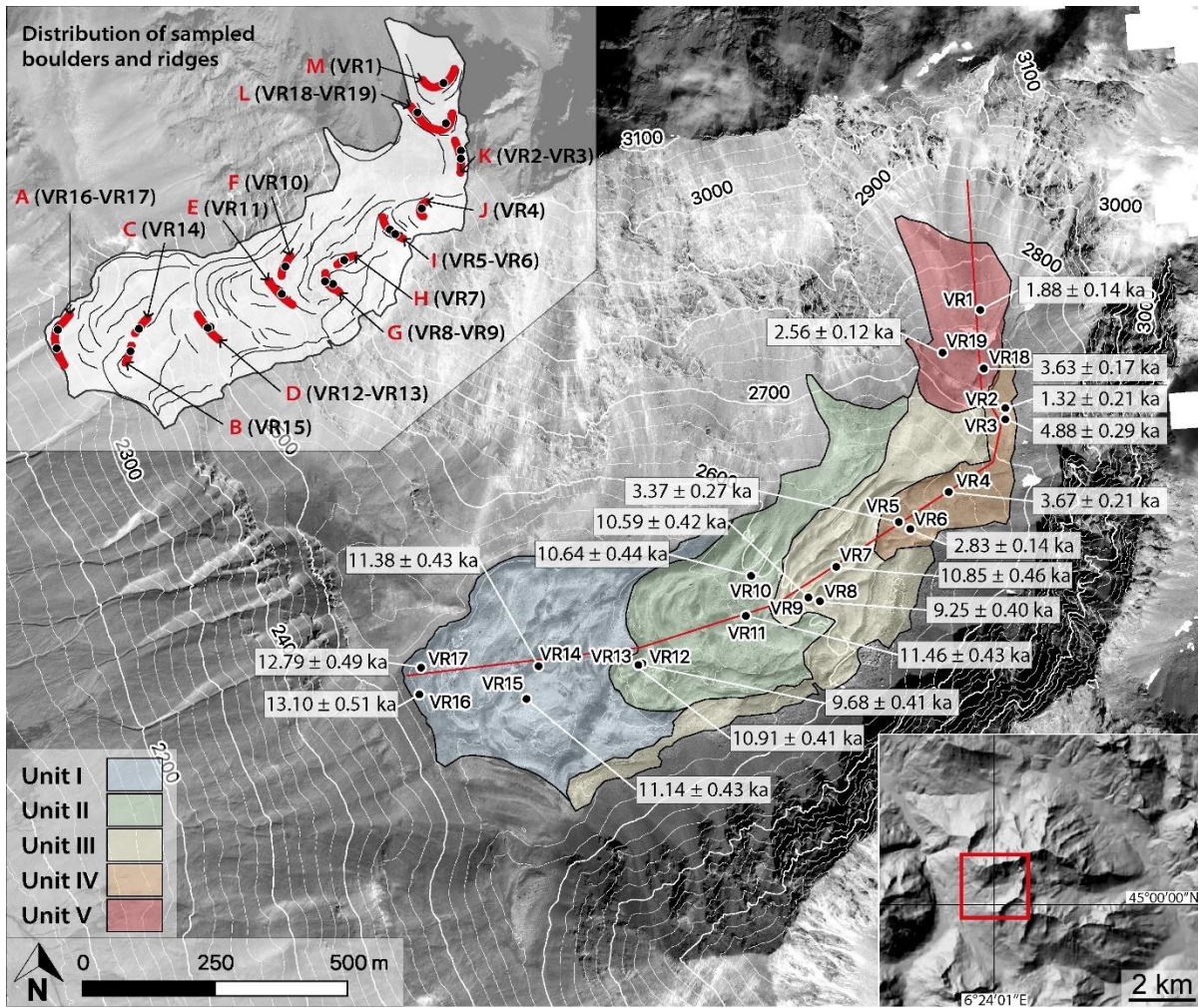
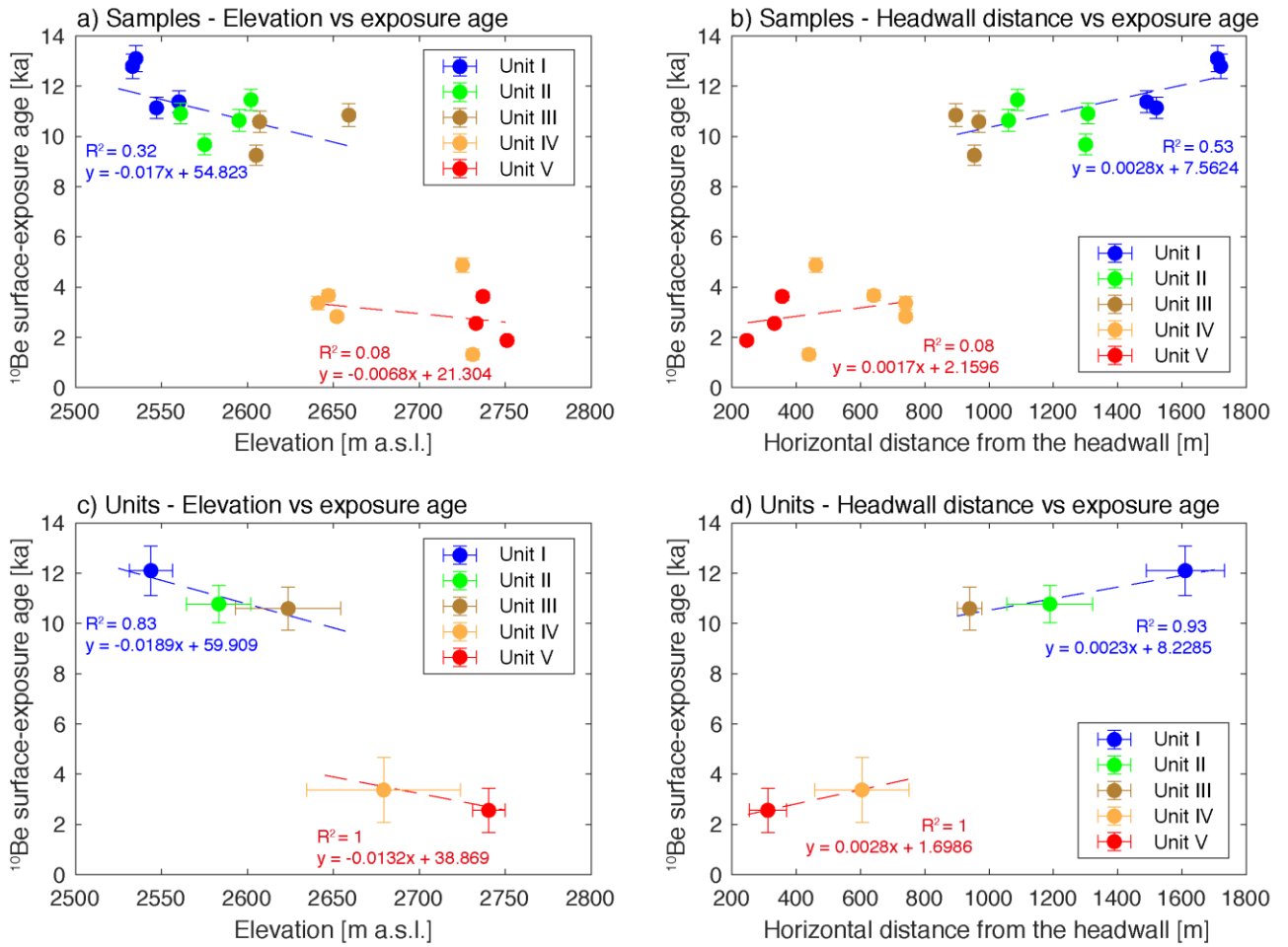
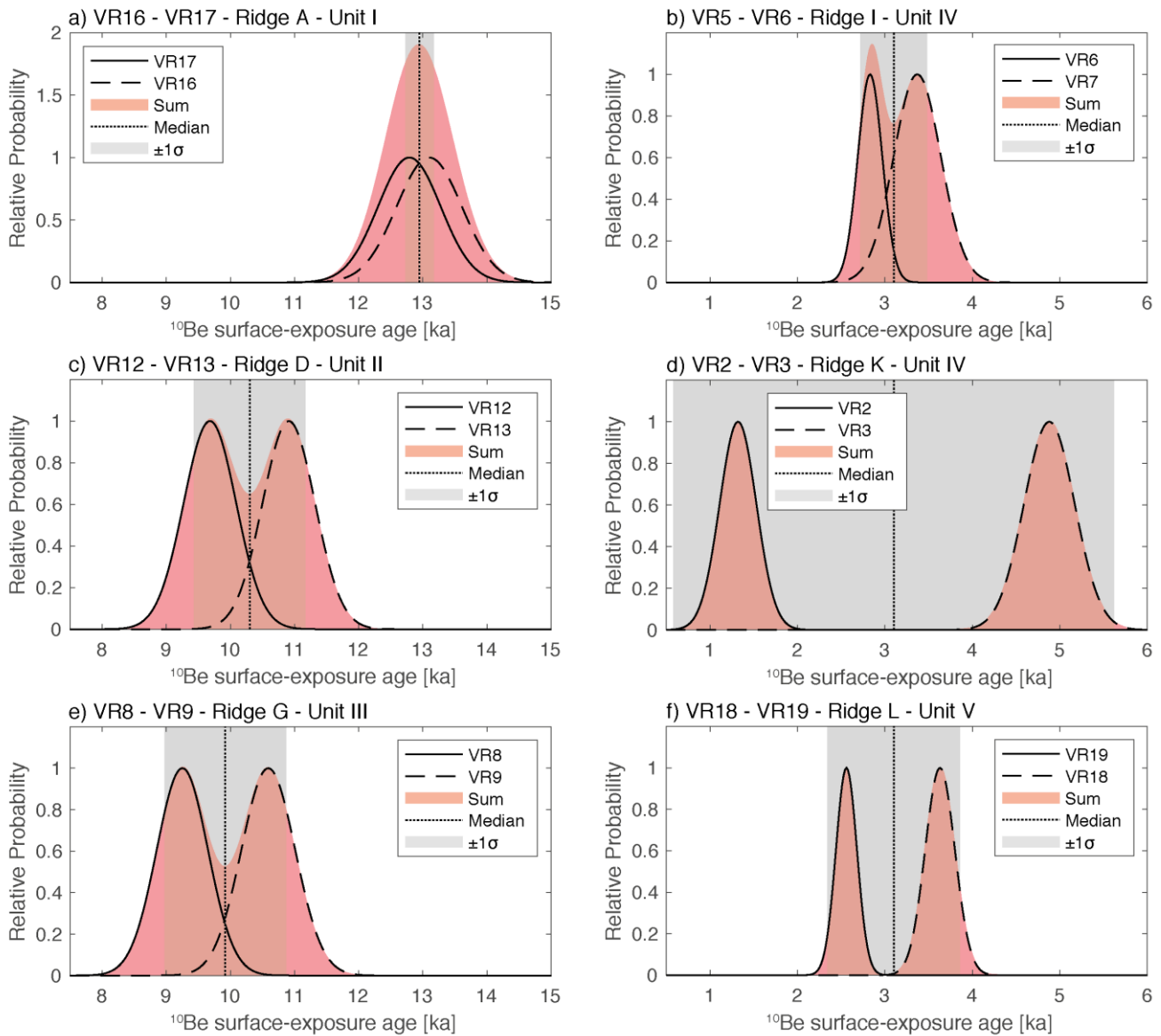


Figure 6: Map of the Vallon de la Route rock glacier, with units and sample locations. Hillshade DEM has been produced from Lidar scanning with 0.5-m resolution; white lines show elevation isolines. Red line is the longitudinal transect used to extract surface displacement (Figure 5a). Individual ^{10}Be surface-exposure ages are shown with one standard deviation (Table 2). The lower right inset shows the location of the study area within the Combeynost massif (red box). Upper left inset shows the samples (black dots) and ridges (red lines) distributed over the main furrow structures (black lines).

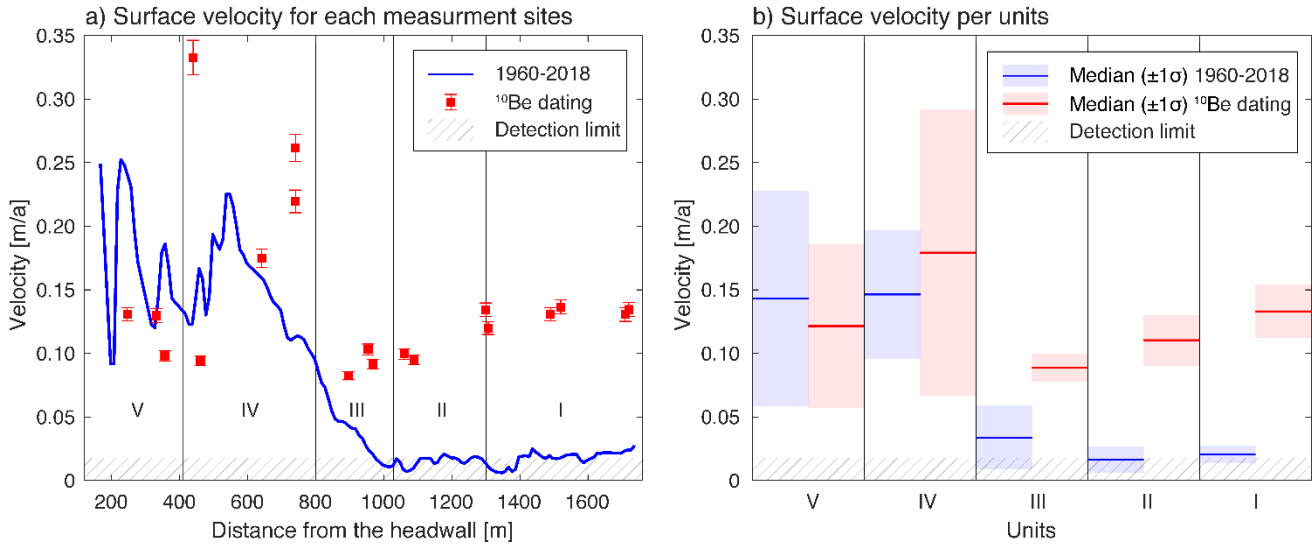
1000



1005 **Figure 7:** ^{10}Be surface-exposure ages of individual samples (a, b) and units (c, d, median values) plotted against elevation (left panels) and horizontal distance to the headwall (right panels). The red and blue dashed lines represent the linear regressions for cluster 1 (Units I, II and III) and 2 (Units IV and V), respectively.



1010 **Figure 8: Probability distributions of the individual ^{10}Be surface-exposure ages, sum and median for each ridge (similar results in Figure A4 for each unit in Supplementary material).**



1015 **Figure 9: a. Rock glacier surface velocity from ^{10}Be surface-exposure dating (distance from the headwall divided by the ^{10}Be surface-exposure age, red squares) and from orthoimage correlation (IMCORR, SAGA package in QGIS, 1960-2018 interval, blue line). b. Median surface velocities are presented for each independent method and each individual unit with their standard deviation ($\pm 1\sigma$). The dashed pattern represents the detection limit (0.026 m/a) defined by median value of the control areas on Figure 3 (used as a threshold value to detect rock glacier surface movement).**

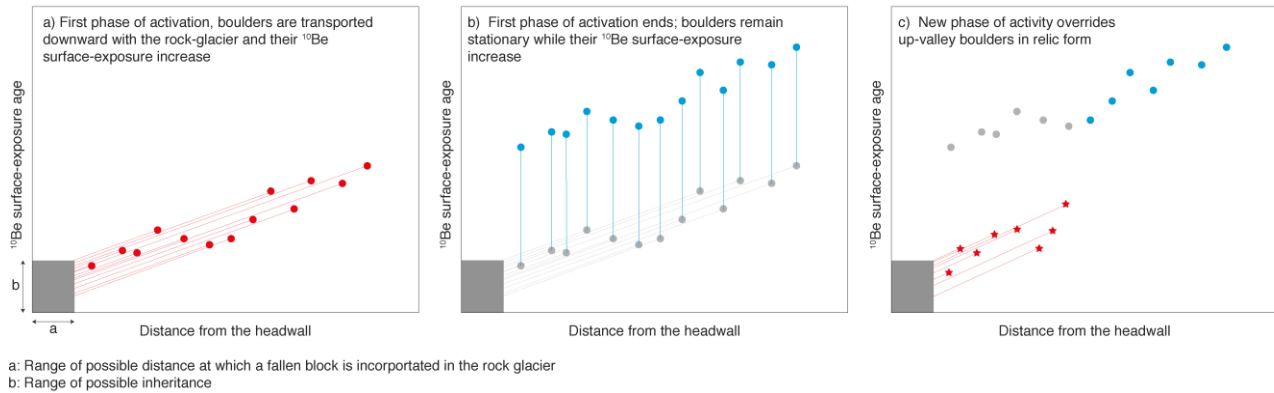
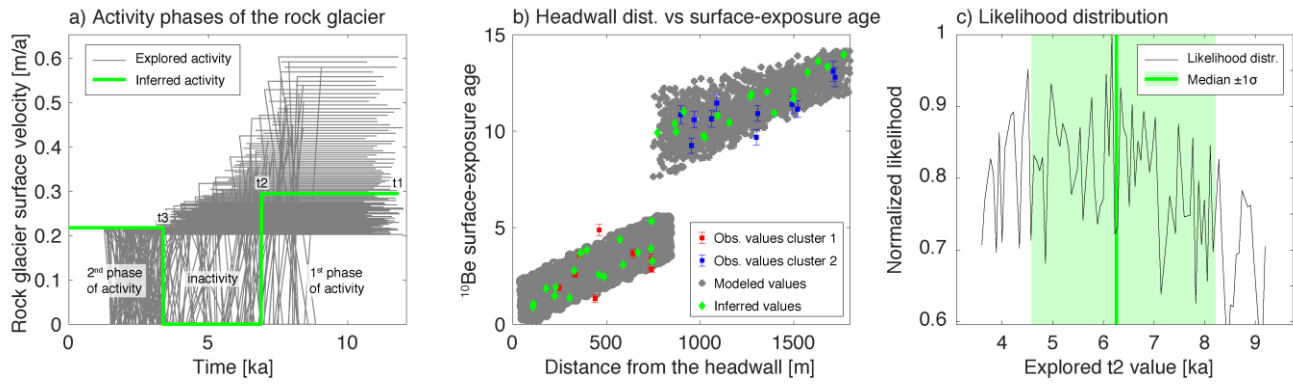


Figure 10: Schematic interpretation of the evolution of the ^{10}Be surface-exposure age patterns as a function of distance from the headwall, considering two phases of rock-glacier activity and stochastic rockfall delivery of boulders. See section 5.3 for details.



1020

Figure 11: a) Activity phases of the rock glacier defined as the evolution of the rock glacier surface velocity in time (explored histories and best-fitting history are shown respectively grey and green lines). b) Relationship between ^{10}Be surface-exposure age and distance to the headwall. Observed values of the cluster 1 and 2, respectively in red and blue squares. Modelled and best-fitting values in grey and green respectively. c) Likelihood distribution of the inversion exploring the time at which the 1st phase of activity ends (t_2). See text for details.

1025

Table 1: Geographic details within the rock glacier system of the Vallon de la Route (Combeynot massif, France) of the samples collected for ^{10}Be surface-exposure dating. Units are area of the rock glacier that have been defined geomorphologically. Ridges are also indicated (Figure 3), on 6 of them two replicate boulders have been sampled. Ridge code goes from A at the lowest elevation to M at the highest elevation. The distance to the headwall has been measured following the centre line of the rock glacier starting at the foot of the headwall (red line in Figures 3 and 6).

Sample ID	Latitude [dec°]	Longitude [dec°]	Elevation [m a.s.l.]	Distance to the headwall [m]	Height of the sample from the ground [cm]	Unit	Ridge
VR1	45.0081	6.4088	2751	246	130	V	M
VR2	45.0064	6.4093	2731	356	220	IV	K
VR3	45.0063	6.4093	2725	332	230	IV	K
VR4	45.0051	6.4079	2647	439	240	IV	J
VR5	45.0046	6.4068	2641	461	300	IV	I
VR6	45.0045	6.4069	2652	641	150	IV	I
VR7	45.0039	6.4051	2659	740	240	III	H
VR8	45.0033	6.4047	2605	740	240	III	G
VR9	45.0034	6.4044	2607	896	150	III	G
VR10	45.0038	6.4031	2595	954	210	II	F
VR11	45.0031	6.4029	2602	968	400	II	E
VR12	45.0024	6.4004	2575	1060	320	II	D
VR13	45.0024	6.4003	2561	1088	500	II	D
VR14	45.0024	6.3979	2560	1300	160	I	C
VR15	45.0019	6.3976	2547	1307	400	I	B
VR16	45.0020	6.3950	2535	1490	160	I	A
VR17	45.0025	6.3951	2533	1520	180	I	A
VR18	45.0071	6.4089	2737	1710	70	V	L
VR19	45.0074	6.4079	2733	1720	100	V	L

1035 **Table 2: Sample details, analytical data related to ^{10}Be measurements and surface-exposure ages for the rock glacier system of the**
Vallon de la Route (Combeynot massif, France), and inputs for Crep calculator (crep.otelo.univ-lorraine.fr; Martin et al.,
2017). We used the production rate (4.16 ± 0.10 at/g/a) derived by Claude et al. (2014) at the Chironico landslide site. The ^{10}Be
surface-exposure ages are presented with $\pm 1\sigma$ external error and $\pm 1\sigma$ internal error (in brackets). Shielding correction includes the
topographic shielding due to surrounding landscape and the dip of the sampled surface calculated with the online calculators
1040 **CRONUS-Earth online calculators (Balco et al., 2008, <http://hess.ess.washington.edu/math>). The density of the rock boulder**
samples is assumed to be 2.75 g/cm 3 . ^{10}Be concentrations were corrected with blank $^{10}\text{Be}/^9\text{Be}$ ratio of $6.28 \pm 0.534 \times 10^{-15}$. Snow-
cover correction was calculated using Gosse and Phillips (2001) equation with snow density of 0.3 g cm $^{-3}$, an attenuation length for
fast neutrons in snow of 150 g cm $^{-2}$ and a cover of 50 cm of snow for 6 months of the year.

Sample ID	Thickness [cm]	Shielding factor	Quartz weight [g]	Carrier [m ^9Be]	$^{10}\text{Be}/^9\text{Be}$ $\times 10^{-14}$	[^{10}Be] [$\times 10^3$ at/g]	^{10}Be surface-exposure age [ka]	Snow corrected ^{10}Be surface-exposure age [ka]
VR1	3	0.87	19.61	0.5115	3.84 ± 0.20	55.9 ± 3.7	1.88 ± 0.14 (0.13)	2.04 ± 0.15 (0.14)
VR2	3	0.92	17.79	0.5073	2.82 ± 0.33	41.7 ± 6.5	1.32 ± 0.21 (0.21)	1.43 ± 0.23 (0.23)
VR3	5	0.91	26.18	0.5114	11.58 ± 0.62	142.6 ± 8.1	4.88 ± 0.29 (0.27)	5.25 ± 0.30 (0.28)
VR4	3	0.93	16.12	0.5100	5.65 ± 0.24	105.9 ± 5.3	3.67 ± 0.21 (0.19)	3.96 ± 0.22 (0.20)
VR5	3	0.93	19.01	0.5102	5.99 ± 0.39	96.0 ± 7.2	3.37 ± 0.27 (0.26)	3.63 ± 0.29 (0.28)
VR6	3	0.92	19.74	0.5121	5.33 ± 0.18	81.4 ± 3.4	2.83 ± 0.14 (0.12)	3.07 ± 0.15 (0.13)
VR7	3	0.93	13.29	0.5100	13.48 ± 0.47	32.9 ± 12.3	10.85 ± 0.46 (0.38)	11.64 ± 0.50 (0.42)
VR8	4	0.94	20.50	0.5106	16.75 ± 0.53	267.8 ± 8.9	9.25 ± 0.40 (0.32)	9.99 ± 0.39 (0.32)
VR9	4	0.93	23.10	0.5102	21.46 ± 0.70	306.8 ± 10.4	10.59 ± 0.42 (0.35)	11.37 ± 0.44 (0.36)
VR10	2	0.96	19.72	0.5110	19.13 ± 0.66	319.8 ± 11.5	10.64 ± 0.44 (0.38)	11.44 ± 0.46 (0.38)
VR11	4	0.95	17.48	0.5095	18.09 ± 0.56	339.5 ± 10.9	11.46 ± 0.43 (0.35)	12.37 ± 0.50 (0.40)
VR12	3	0.96	18.34	0.5104	15.88 ± 0.53	283.0 ± 10.0	9.68 ± 0.41 (0.34)	10.43 ± 0.43 (0.35)
VR13	3	0.93	22.29	0.5110	20.78 ± 0.64	308.1 ± 9.9	10.91 ± 0.41 (0.33)	11.71 ± 0.46 (0.37)
VR14	3	0.96	18.04	0.5100	18.34 ± 0.56	333.9 ± 10.8	11.38 ± 0.43 (0.34)	12.28 ± 0.50 (0.40)
VR15	3	0.97	18.81	0.5090	18.74 ± 0.61	326.8 ± 11.1	11.14 ± 0.43 (0.35)	11.98 ± 0.50 (0.41)
VR16	3	0.95	17.26	0.5092	19.66 ± 0.61	374.5 ± 12.2	13.10 ± 0.51 (0.40)	14.09 ± 0.55 (0.44)
VR17	4	0.97	19.76	0.5089	22.07 ± 0.68	368.3 ± 11.8	12.79 ± 0.49 (0.39)	13.75 ± 0.53 (0.42)
VR18	3	0.91	18.78	0.5086	6.68 ± 0.22	109.3 ± 4.2	3.63 ± 0.17 (0.14)	3.92 ± 0.18 (0.15)
VR19	3	0.91	21.18	0.5094	5.40 ± 0.17	76.5 ± 3.0	2.56 ± 0.12 (0.11)	2.76 ± 0.13 (0.11)

1045 **Table 3: ^{10}Be surface-exposure ages for each ridge of the rock glacier system of the Vallon de la Route (Combeynot massif, France). n represents the number of samples per ridge. For the ridges with replicates, the median values are reported with the standard variation $\pm 1\sigma$. For the inheritance estimate, the difference in ^{10}Be concentration of each pair of replicates has been used and ^{10}Be surface-exposure ages have been recalculated assuming origin from the headwall (at an elevation of 2997 m a.s.l.).**

Ridge ID	Corresponding sample	Mean elevation [m a.s.l.]	Mean distance to the headwall [m]	^{10}Be surface-exposure age		Variability [%]	Inheritance est. $\pm 1\sigma$ [ka]
				Median	$\pm 1\sigma$ [ka]		
A (n=2)	VR16 - VR17	2534	1715	12.95	± 0.22	2	0.17 ± 0.01
B (n=1)	VR15	2547	1520	11.14	± 0.43		
C (n=1)	VR14	2560	1490	11.38	± 0.43		
D (n=2)	VR12 - VR13	2568	1303	10.30	± 0.87	8	0.67 ± 0.03
E (n=1)	VR11	2602	1088	11.46	± 0.43		
F (n=1)	VR10	2595	1060	10.64	± 0.44		
G (n=2)	VR8 - VR9	2606	961	9.92	± 0.95	10	1.06 ± 0.04
H (n=1)	VR7	2659	896	10.85	± 0.46		
I (n=2)	VR5 - VR6	2646	740	3.10	± 0.38	13	0.39 ± 0.03
J (n=1)	VR4	2647	641	3.67	± 0.21		
K (n=2)	VR2 - VR3	2728	450	3.10	± 2.52	99	2.88 ± 0.47
L (n=2)	VR18 - VR19	2735	344	3.10	± 0.76	26	0.88 ± 0.40
M (n=1)	VR1	2751	246	1.88	± 0.14		

1050 **Table 4: Median value of the ^{10}Be surface-exposure ages for each unit of the rock glacier system of the Vallon de la Route (Combeynot massif, France). n represents the number of samples per unit. Surface velocity calculated from ^{10}Be surface-exposure dating (distance from the headwall divided by ^{10}Be surface-exposure age) and from image correlation (IMCORR, SAGA package on QGIS) of orthoimages (1960-2018 interval).**

Unit ID	Mean elevation $\pm 1\sigma$ [m a.s.l.]	Mean distance to the headwall $\pm 1\sigma$ [m]	^{10}Be surface-exposure age		Displacement 1960-2018 Median $\pm 1\sigma$ [m]	Integrated velocity $\pm 1\sigma$ [m/a]	
			Median $\pm 1\sigma$ [ka]	Variability [%]		^{10}Be surface-exposure age	1960-2018
Unit I (n=4)	2544 ± 12	1610 ± 122	12.10 ± 0.99	8	1.19 ± 0.40	0.13 ± 0.02	0.02 ± 0.01
Unit II (n=4)	2583 ± 19	1189 ± 133	10.78 ± 0.74	7	0.95 ± 0.60	0.11 ± 0.02	0.02 ± 0.01
Unit III (n=3)	2624 ± 31	939 ± 38	10.59 ± 0.86	8	1.96 ± 1.45	0.89 ± 0.01	0.03 ± 0.03
Unit IV (n=5)	2679 ± 45	604 ± 147	3.37 ± 1.30	44	8.49 ± 2.93	0.18 ± 0.11	0.15 ± 0.05
Unit V (n=3)	2740 ± 9	311 ± 58	2.56 ± 0.88	34	8.30 ± 4.90	0.12 ± 0.06	0.14 ± 0.08

1055

1060

1065

Appendix

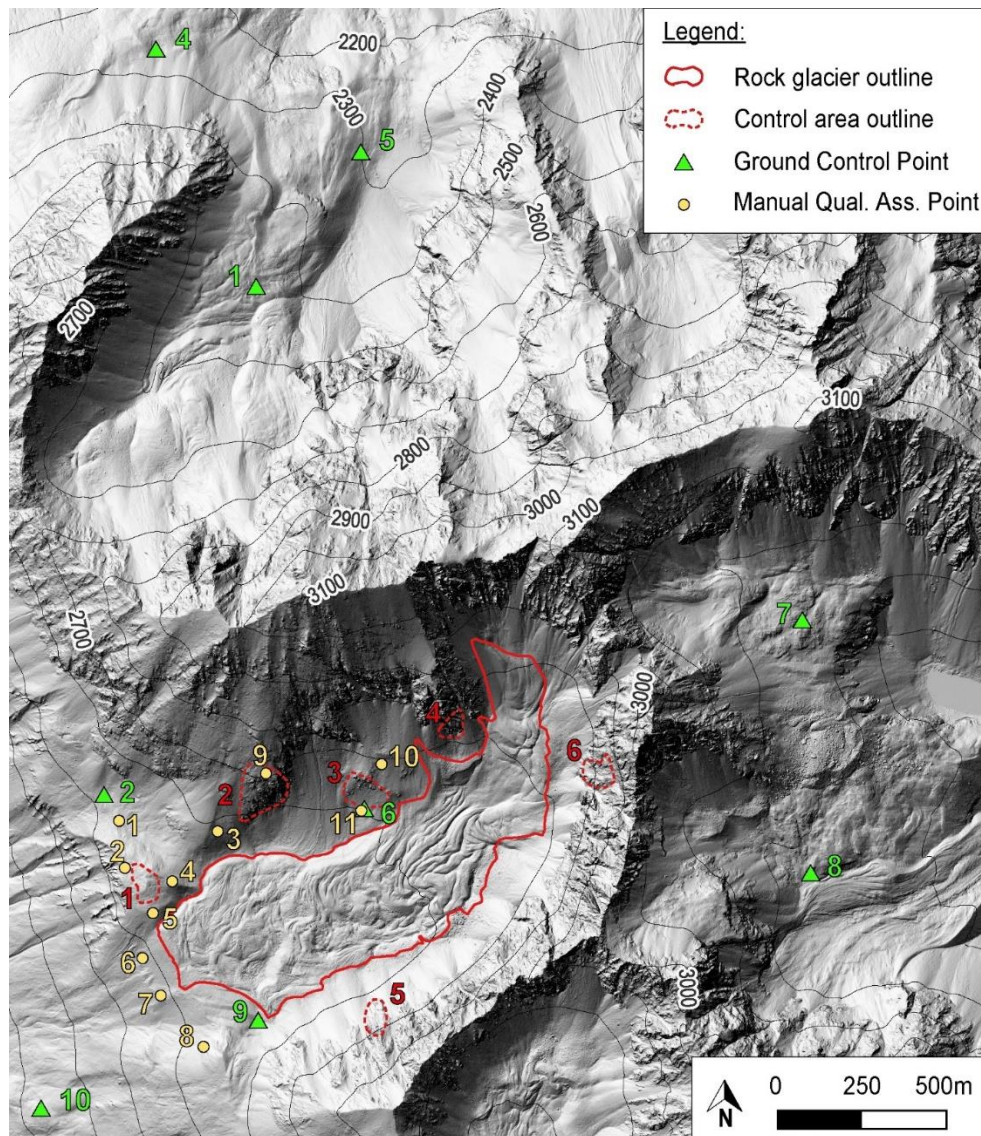
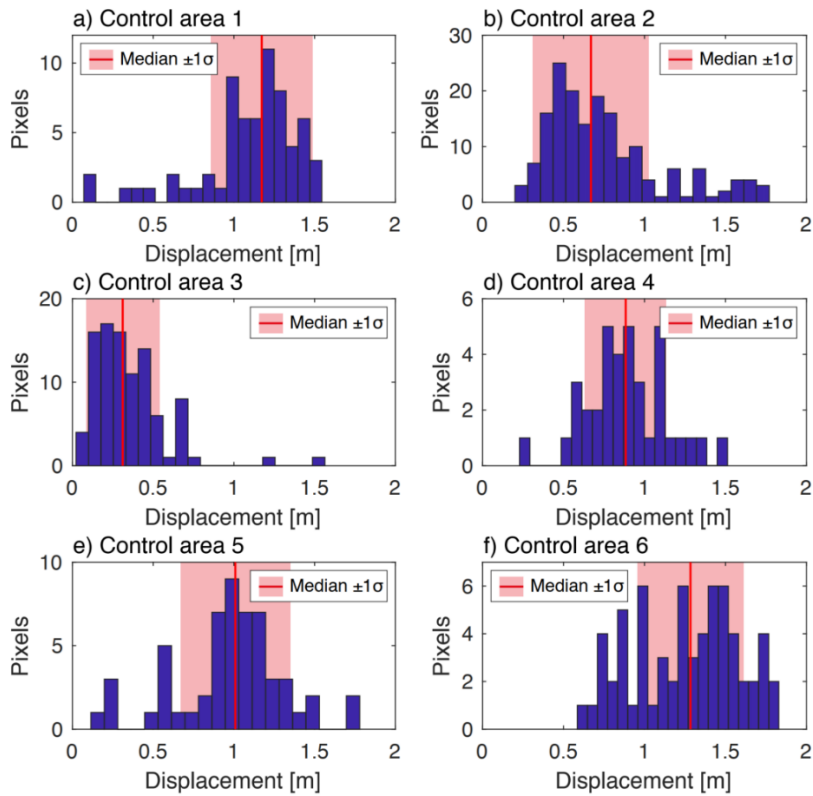
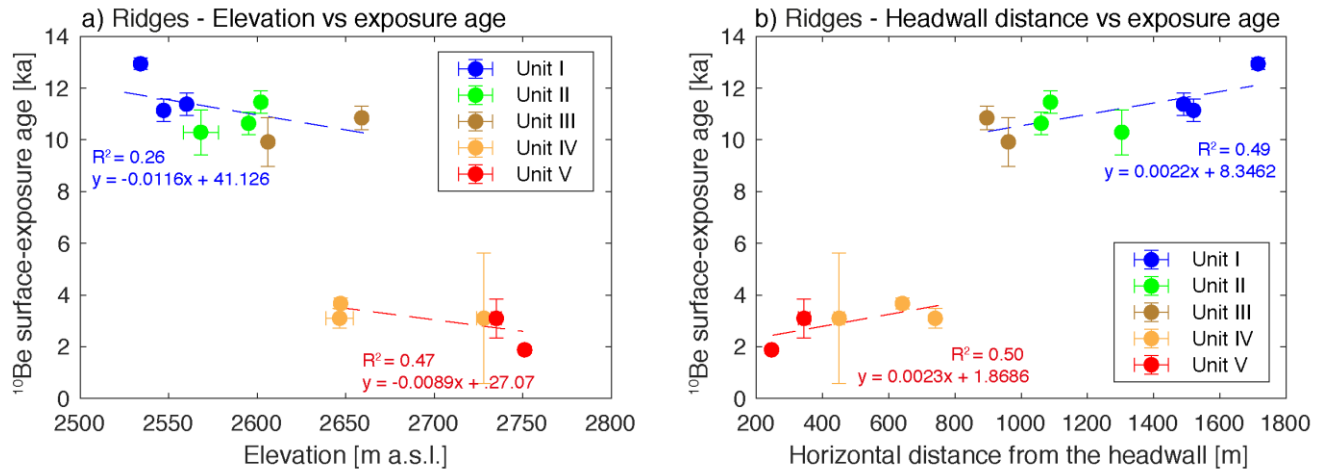


Figure A1: Map showing the location of the ground control points, the control areas and the manual control points used in the remote-sensing analysis.



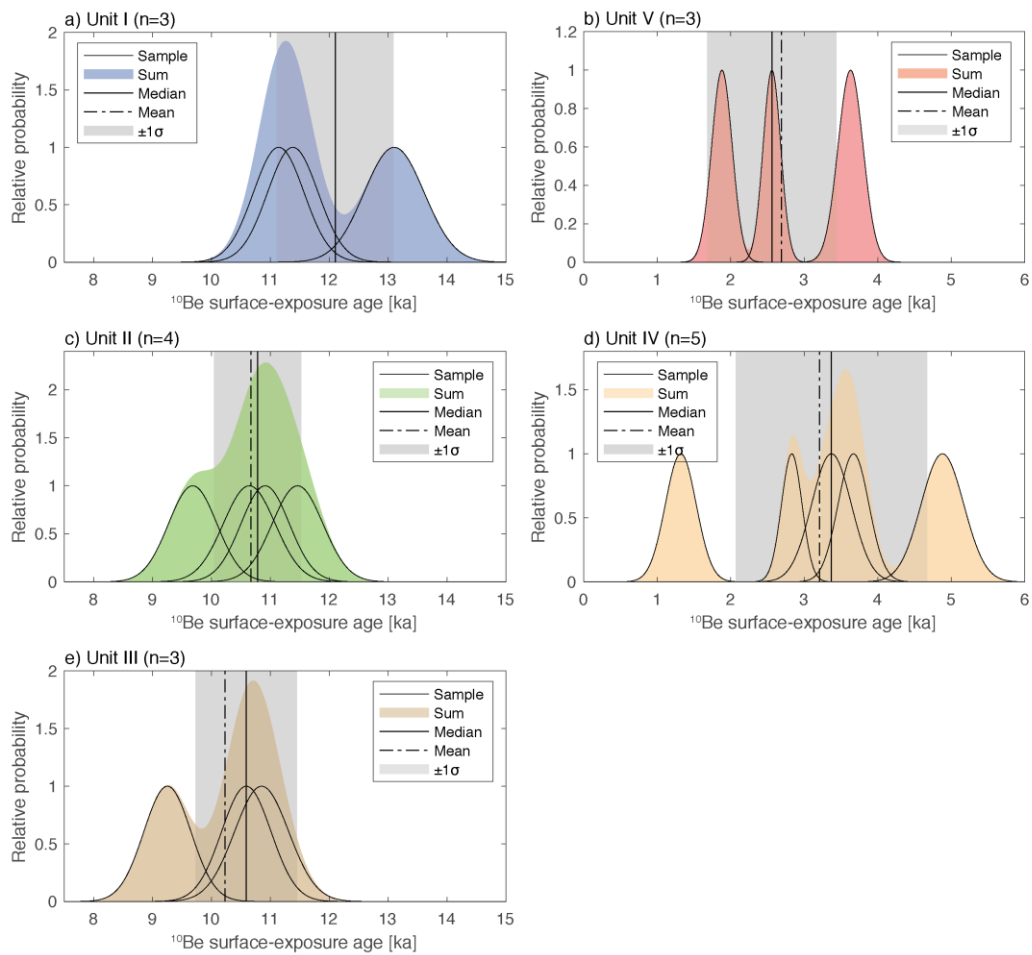
1070

Figure A2: Histograms and median values of the surface displacement for each control area as shown in Figures 3 and A1.



1075

Figure A3: ^{10}Be surface-exposure ages of individual ridges (a,b), plotted against elevation (a) and horizontal distance to the headwall (b). The red and blue dashed lines represent the linear regressions for cluster 1 (Units I, II and III) and 2 (Units IV and V), respectively.



1080 **Figure A4: Probability distributions of the ^{10}Be surface-exposure ages for individual samples with sum, mean, median and standard deviation for each unit.**

Table A1: Statistics of the ground control points (GCP) used for the co-registrations of the two orthomosaics. Coordinates are mentioned in the EPSG:2154 - RGF93 v1 / Lambert-93 system.

ID	X/Easting	Y/Northing	Z/Altitude [m a.s.l.]	Accuracy X/Y/Z [m]	Error [m]	X error [m]	Y error [m]	Z error [m]	X est	Y est	Z est
GCP1	967692.6055	6441333.13	2445.72998	0.5	0.44	0.33	0.17	0.25	967692.93	6441333.30	2445.98
GCP2	967241.2324	6439828.326	2510.1001	0.5	0.11	0.06	0.04	-0.09	967241.29	6439828.36	2510.01
GCP3	966734.1818	6440583.405	2476.37012	0.5	0.46	-0.30	0.34	0.04	966733.88	6440583.74	2476.41
GCP4	967396.0163	6442035.338	2268.51001	0.5	0.17	0.07	0.08	-0.13	967396.08	6442035.42	2268.38
GCP5	968002.852	6441731.952	2301.87988	0.5	1.03	-0.71	-0.53	-0.53	968002.14	6441731.42	2301.35
GCP6	968011.3061	6439787.281	2603.13989	0.5	0.97	-0.50	0.54	-0.64	968010.81	6439787.82	2602.50
GCP7	969309.2	6440344.9	2749.7099	0.5	0.68	0.50	-0.39	0.26	969309.70	6440344.51	2749.97
GCP8	969334.57	6439595.47	2677.85	0.5	0.45	0.09	0.43	-0.08	969334.66	6439595.90	2677.77
GCP9	967699.3	6439158	2550.9899	0.5	0.94	-0.90	0.23	-0.15	967698.40	6439158.23	2550.84
GCP10	967056.4	6438897	2231.2299	0.5	1.11	0.72	-0.84	-0.12	967057.12	6438896.16	2231.11
Median $\pm 1\sigma$ [m]					0.57 ± 0.34						

1085

Table A2: Results of the manual control points assessment between the orthomosaics of 1960 and 2018. Locations of the points are shown in Figures 3 and A1. Coordinates are mentioned in the EPSG:2154 - RGF93 v1 / Lambert-93 system.

ID	Ref. year	1960		2018		Y diff [m]	X diff [m]	Distance [m]	
		Y Coord.	X Coord.	Y Coord.	X Coord.				
1	1960	6439755.99	967286.309	6439756.8	967287.176	-0.81	-0.87	1.19	
2	2018	6439617.448	967304.239	6439617.101	967303.589	0.35	0.65	0.74	
3	2018	6439724.814	967578.359	6439725.682	967579.053	-0.87	-0.69	1.11	
4	1960	6439577.379	967444.676	6439577.9	967445.254	-0.52	-0.58	0.78	
5	1960	6439482.492	967386.922	6439483.403	967387.356	-0.91	-0.43	1.01	
6	2018	6439348.534	967357.207	6439350.009	967356.686	-1.47	0.52	1.56	
7	2018	6439237.047	967410.044	6439238.869	967410.477	-1.82	-0.43	1.87	
8	2018	6439087.211	967537.061	6439087.992	967537.755	-0.78	-0.69	1.04	
9	2018	6439897.034	967721.948	6439895.646	967722.728	1.39	-0.78	1.59	
10	2018	6439925.404	968064.174	6439924.667	968064.218	0.74	-0.04	0.74	
11	1960	6439786.761	968010.643	6439786.862	968010.845	-0.10	-0.20	0.23	
Median $\pm 1\sigma$ [m]								1.04 ± 0.45	

1090

Table A3: Statistics of the rock glacier, units, and control areas from the IMCORR analysis. Total area of both orthomosaics is 3067391 m².

	n	% of the total orthomosaic area	Area [m ²]	Surface displacement between 1960-2018 [m]			
				Median $\pm 1\sigma$	Mean	Minimum	Maximum
Rock glacier	4181	15.54	476648	1.30 ± 2.01	2.37	0.02	20.41
Unit I	1500	4.95	151798	1.19 ± 0.40	1.22	0.07	5.38
Unit II	1155	4.09	125560	0.95 ± 0.60	1.08	0.02	13.28
Unit III	971	3.57	109624	1.96 ± 1.45	2.19	0.12	13.28
Unit IV	321	1.25	38363	8.49 ± 2.93	8.59	2.86	17.28
Unit V	234	1.68	51595	8.30 ± 4.90	8.39	0.29	20.41
Control 1	65	0.22	6654	1.17 ± 0.32	1.09	0.07	1.54
Control 2	170	0.56	17132	0.67 ± 0.36	0.75	0.20	1.77
Control 3	96	0.32	9964	0.31 ± 0.23	0.36	0.02	1.56
Control 4	37	0.14	4228	0.88 ± 0.25	0.89	0.23	1.51
Control 5	55	0.18	5547	1.01 ± 0.34	0.98	0.11	1.78
Control 6	65	0.21	6536	1.28 ± 0.33	1.26	0.59	1.83
Control all	488	1.63	50061	0.79 ± 0.43	0.82	0.02	1.83